Charged Kaon Ratios and Yields Measured with the STAR Detector at the Relativistic Heavy Ion Collider

By

C.L. Kunz

B.S. Chemistry, McPherson College, 1997

Submitted in Partial Fulfillment of the

Requirement for the Degree of

Doctor of Philosophy

Department of Chemistry

Carnegie Mellon University

Pittsburgh, Pennsylvania 15213

September 2003

This thesis is dedicated to my parents for their guidance and support. They have long been two of my best friends. Without them, I would not be here.

Table of Contents

List of Tables

List of Figures

Acknowledgments

I would like to thank my research advisor, Professor Morton Kaplan, for his support, guidance, and patience. He has encouraged me to take advantage of opportunities that I never thought possible. I would also like to thank Dr. Nu Xu who provided me with advice and guidance on my research. He has assisted a great deal in my physics knowledge.

I would also like to thank Dr. Zoran Milosevich and Dr. Jack Engelage. They provided me with insight and understanding of the STAR experiment as well as their friendship.

I wish to express my appreciation to my committee members: Dr. Morton Kaplan, Dr. Paul Karol, Dr. Hyung Kim, and Dr. Curtis Meyer, for their encouragement and keeping me on the right track as I progressed through my graduate school career.

I would like to acknowledge Carnegie Mellon University, and specifically the chemistry department, for providing the opportunity and support that has enabled me to participate in groundbreaking research.

I also appreciate the hospitality extended by the Relativistic Nuclear Collisions Group at Lawrence Berkeley National Laboratory during my extended visits. Their support was essential to the completion of my analysis.

I would like to thank the STAR Collaboration for providing the data production and software analysis tools. I would also like to thank the STAR Operations Group for the excellent functioning of the detector and associated hardware.

I would like to thank the RHIC Operations Group for their hard work to provide collisions to the experiments.

I would also like to acknowledge the U.S. Department of Energy for financial support through Research Grant DE-FG02-87ER40324 with Carnegie Mellon University.

I would also like to thank all of my teachers over the years. Their patience and persistence have greatly contributed to my academic career. I would especially like to single-out my science teachers whose enthusiasm for learning was contagious.

And last, but not least, I would like to thank my family and friends for their support and friendship during my long and sometimes difficult journey. They helped provide me with motivation and enabled me to maintain what little sanity I have left.

Abstract

The mid-rapidity charged kaon ratios and yields are reported for the 200 AGeV Au+Au, 130 AGeV Au+Au, and 200 GeV pp data sets. The K^{-}/K^{+} ratios are shown to be flat as a function of rapidity, transverse momentum, and centrality for the ranges investigated. The integrated ratios are 0.928 ±0.0028 (stat.) ±0.03 (sys.), 0.953 ±0.0.0012 (stat) ±0.01 (sys.), and 0.964 ±0.0039 (stat.) ±0.01 (sys.) for 130 AGeV Au+Au, 200 AGeV Au+Au, and 200 GeV pp respectively. Thermal fits are applied to the ratios to extract the baryo-chemical potential and chemical freeze-out temperature. The baryo-chemical potential, as well as the kaon ratio, suggest that the net-baryon density at mid-rapidity is approaching zero at RHIC energies. A quark coalescence model suggests quark degrees of freedom are important in the formation of the ratios. The corrected yields are fit with an exponential in m_t and the dN/dy and inverse slope parameter are extracted. The inverse slope parameter is used along with the average collective flow velocity in a simple relationship to extract the thermal freeze-out temperature. A more sophisticated hydrodynamically motivated fit, using pion, kaon, and proton data, shows agreement with the trend from this simple relationship.

Section 1

1.1 Introduction

In 1911, during an experiment scattering α-particles off gold foil, Rutherford was led to a theoretical picture of an atom [Rut11]. In order to explain the behavior of the α-particle, including a large angle scattering seen by a very few α-particles, he suggested the positive charge of the atom was entirely held in the center of the atom in the nucleus. In his 1911 paper, he considered the nucleus as a point charge:

> "We shall suppose that for distances less than 10^{-12} cm. the central charge and also the charge on the alpha particle may be supposed to be concentrated at a point. [Rut11]"

Rutherford's atom was made up of a nucleus of Z positive charges and A-Z pairs of positive and negative charges surrounded by a sphere of Z uniformly distributed electrons, which had been known since 1898. This was a big step toward understanding matter and the beginning of a new field, nuclear physics. As the field progressed, higher energy probes were needed to study the smaller and smaller structures of nuclear matter. The continuing development of particle accelerators enabled the study of ever-smaller length scales.

Nuclear structure was still not well understood when in 1932 Chadwick discovered the neutron [C32]. It became apparent that the nucleus is built up of protons and neutrons. More exotic particles were soon found, such as muons and pions. The observation of these particles was followed by the discovery of related mesons and a large number of baryons. It was suggested by Gell-Mann and Zwieg, that these particles may be composed of more elementary particles [Gel64, Zwe64].

The first evidence for the existence of quarks came in 1966 during a Stanford Linear Accelerator Center experiment probing the internal structure of nucleons via deep-inelastic electron scattering [Bre69]. According to our current understanding, the constituents of hadrons are quarks and leptons interacting via gluons and photons. Currently we have found:

$$\begin{array}{ccccccc} & \text{quarks} & & & & \text{leptons} & \\ u & c & t & \text{and} & e & \mu & \tau \\ d & s & b & & \nu_e & \nu_\mu & \nu_\tau \end{array}$$

There are six types of quarks: u – up, c – charm, t – top, have a $+\frac{2}{3}$ charge, and s – strange, d – down, b – bottom, have a $-\frac{1}{3}$ charge. The quarks are arranged in pairs of nearly equal mass, (u,d), (c,s), and (t,b). The leptons are also arranged in pairs, (e,ν_e), (μ,ν_μ), and (τ,ν_τ). All of these particles also have a corresponding anti-particle and each quark has a color charge – red (anti-red), green (anti-green), or blue (anti-blue). Baryons consist of 3 quarks or anti-quarks (or a mix), and mesons are made up of a quark and an anti-quark. All nuclear matter that we can detect must be colorless, e.g. a baryon must contain red, green and blue (or $\overline{r}\overline{g}\overline{b}$) and mesons must contain red, anti-red (or $b\overline{b}$ or $g\overline{g}$).

During the very early expansion of the universe, microseconds after the big bang, the primordial matter must have been very hot and dense. If we extrapolate backward in time from the current background temperature of 2.7 K [Mat90] we find a temperature of

≈200 MeV (10^{12} K) at about 20 μs after the big bang [Kol90]. Did the early universe go through a phase transition? Our knowledge of the space-time evolution of this phase transition could assist in our understanding of the universe we see today.

Accelerators, such as RHIC, have been designed to provide high-energy heavy-ion collisions offering a possible way to create and study the QGP. The collisions produce a hot and dense system that may reach energy densities and temperatures high enough for a phase transition to occur. If this phase transition does occur, the experimental observations will lead to the refinement of QCD or possibly an entirely new theory to describe the behavior of this extreme state of matter.

In this thesis we will first discuss what happens during a heavy ion collision, and the effect of a quark gluon formation on a few of the experimental observables. We will then describe the Relativistic Heavy Ion Collider (RHIC) accelerator and the Solenoidal Tracker at RHIC (STAR) detector. Next we will briefly describe how the data is reconstructed in the detector, and how the particles are identified. In section 6, we will discuss the results of the kaon analysis on ^{197}Au+^{197}Au collisions at 130 AGeV (GeV per nucleon, also GeV/n) and 200 AGeV and pp collisions at 200 GeV. We will then discuss the results of these analyses and present our conclusions.

Section 2

2.1 Quark Deconfinement

Strongly interacting matter is described by the interactions of quarks through the exchange of gluons. The theory that describes these interactions is called quantum chromodynamics (QCD), and it has a coupling constant, α_s, that can be defined as follows:

$$\alpha_s(q^2) \propto \frac{1}{\ln \frac{q^2}{\Lambda^2}}$$

where:

α_s is the coupling constant,

q is the momentum transfer, and

Λ is a dimensional scaling parameter.

At larger momentum transfer, i.e. small length scales, the coupling constant goes to zero ($\alpha_s(q^2) \to 0$) and a perturbative treatment is a good description of the process. At small momentum transfer, therefore large length scales, the coupling constant approaches large values. In this region quark behavior is explained by color confinement and implies that quarks appear as colorless objects. A perturbative treatment, based on an expansion in powers of the coupling constant, is no longer applicable. A non-perturbative treatment is needed.

Debye charge screening is a well-understood process in atomic physics. The Coulomb potential for two charges changes significantly when these charges are placed in an environment with a distribution containing both positive and negative charges, e.g.

a plasma. A similar phenomenon occurs in QCD at extremely high temperatures and extreme nuclear densities. Under these conditions, there is weak coupling. The hadronic matter, normally a color insulator, becomes an ideal color conducting plasma of quarks and gluons. The long-range force becomes Debye screened due to the collective effects, similar to an electromagnetic plasma.

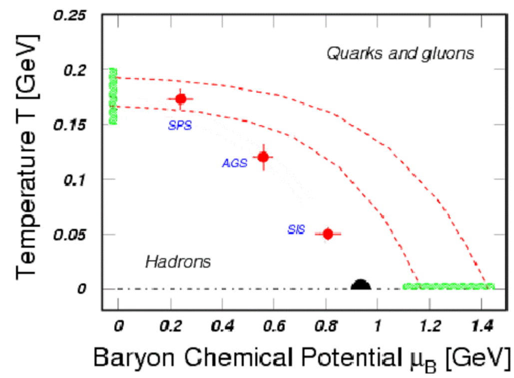

Figure 2.1 Temperature versus Baryo-chemical potential. Will data from RHIC agree with the trend created from lower energy experiments?

If we plot the freeze-out temperature versus the baryo-chemical potential (explained in section 7.2.1) for previous heavy ion experiments, we can see a trend approaching the deconfined region of quarks and gluons (see Fig. 2.1). The dashed lines represent the QCD prediction for the phase transition.

2.2 Space-Time Evolution of Relativistic Heavy Ion Collisions

The nuclear matter in the "participant region" of nucleus – nucleus collisions undergoes intense heating and compression. During these collisions, the energy densities at RHIC reached 4.6 GeV/fm^3 (central 130 AGeV Au+Au collisions [Adc01]) approximately 50% larger than achieved at the SPS [Alb95], compared to 0.15 GeV/fm^3 for normal nuclear matter.

In these high-energy heavy ion collisions it is possible to form a quark-gluon plasma (QGP), which will go through several stages during the space-time evolution. The stages, in chronological order, are: 0) Lorentz contracted ions before the collision,

(1) pre-equilibrium processes and formation by thermalization; possible formation of the QGP, (2) the mixed phase, (3) the hadron gas, and finally (4) the free hadrons.

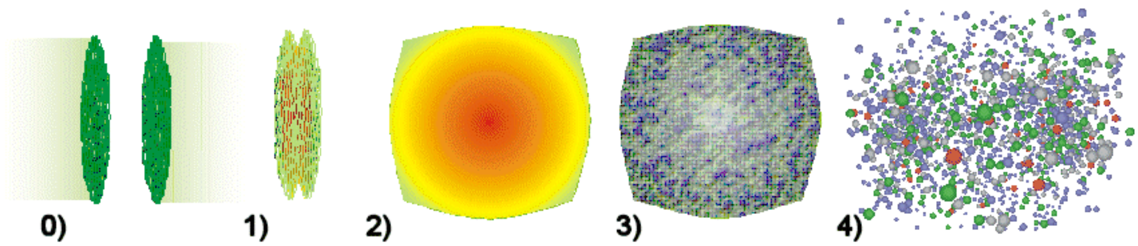

Figure 2.2 Schematic picture of an ultra-relativistic collision. Time is increasing left to right. See text for description of stages.

If we assume thermal equilibrium is attained shortly after the collision occurs, the temperature can be estimated using a hydrodynamic model. The expansion is very likely to be adiabatic, which means no dissipation will occur during the expansion. Therefore isentropic expansion is presumed up to the critical temperature T_c. The temperature in the mixed phase remains constant during an isothermal expansion; the latent heat is absorbed in converting the quarks and gluons into hadrons. At time $\tau_{h,}$ (chemical freeze-out) the hadronization is completed and the hadron gas starts to cool to time τ_f (thermal freeze-out) where the density of the system is low enough for the hadrons to escape (see Fig. 2.3).

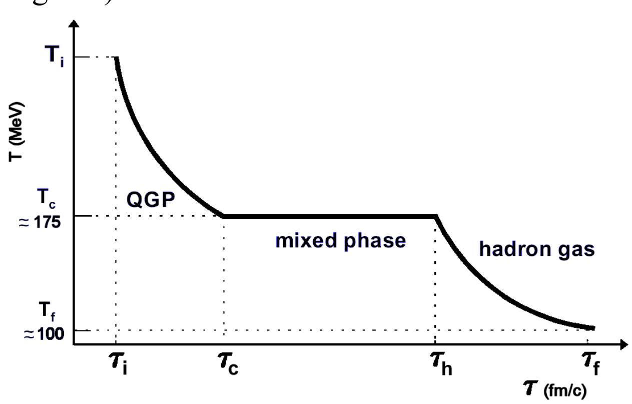

Figure 2.3 Evolution of the QGP in terms of temperature versus time, assuming isentropic and isothermal expansions.

2.2.1 Pre-Equilibrium Processes - Possible Formation of the QGP

There are two extreme points of view of what will happen when heavy ions collide at relativistic energies. These two models, Landau and Bjorken, deal with the amount of nuclear stopping during the collision. Stopping is defined as the percentage of kinetic energy loss by the nucleons in the collision, of crucial importance for the initial energy density and particle density. Figure 2.4 shows the rapidity distribution of: a) the beam nucleons before the collision, b) full stopping (Landau), and c) transparency (Bjorken). Rapidity is a kinematic quantity, derived from velocity (see Appendix A.1).

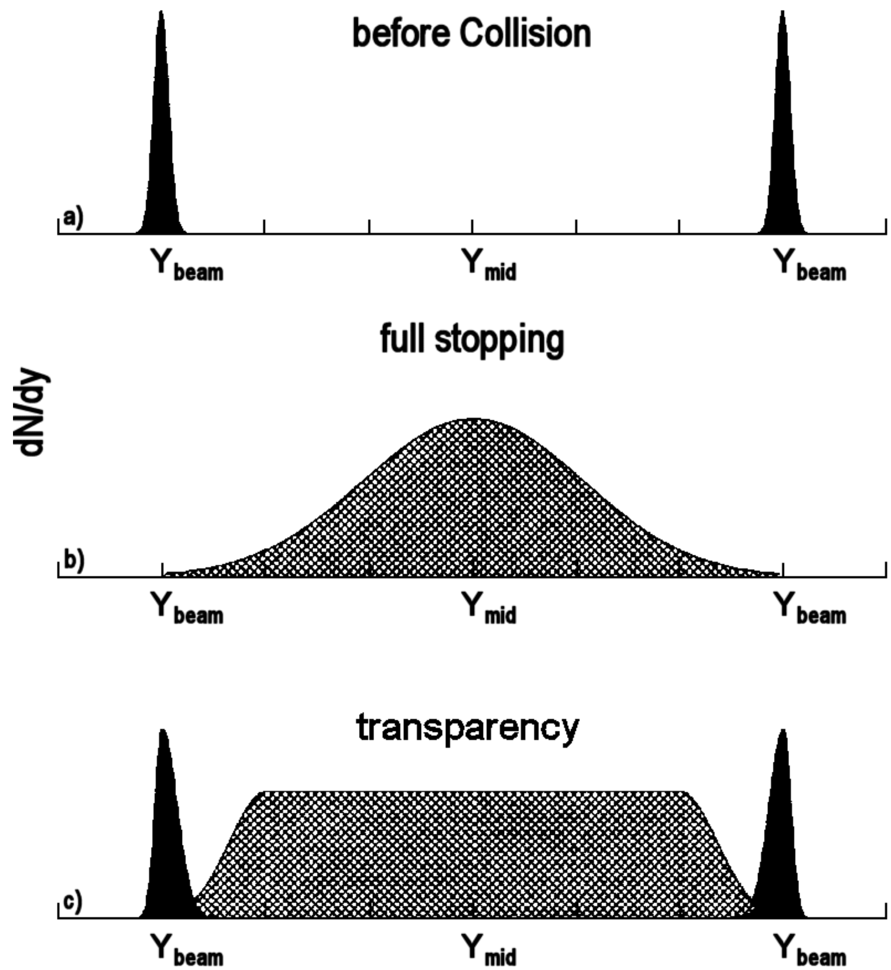

Figure 2.4 Nuclear stopping scenarios. Particle rapidity distributions are presented before (a) and after collision for Landau (b) and Bjorken(c).

At RHIC energies, evidence points toward a Bjorken stopping scenario, however, some stopping is definitely occurring since the net-baryon density is non-zero. The mechanism capable of transporting baryons 5 units of rapidity is still being considered [Van98]. Matter in this space-time region is probably a form of quasi-free quarks and gluons. If the number of interactions between partons is large enough, the pre-equilibrium phase will lead to local thermal equilibrium.

Multiple scattering of the participants will lead to production of more partons, increasing entropy and causing local memory loss. The most critical assumption made so far is that the system lived long enough to achieve both chemical and thermal equilibrium. Thermal equilibrium means that the particle momenta are distributed according to a Boltzmann distribution with a certain temperature. While chemical equilibrium is satisfied when the abundance of the different particle species are given by their relative thermodynamic weight.

2.2.2 Mixed QGP and Hadrons

While the hot dense matter created in the collision expands the system size increases, and the energy density and temperature will decrease as described above (section 2.2.1). At the critical temperature T_c the system enters a mixed partonic-hadronic phase. The larger degrees of freedom of the quarks and gluons are transferred to hadron degrees of freedom at a constant temperature.

2.2.3 Hadron Gas and Free Hadrons

In the hadron gas phase, the temperature will continue to drop until the mean free path of the hadrons exceeds the dynamical size of the system. At this point, the system will undergo thermal freeze-out to a system of free hadrons. These free hadrons are the end product of the collision. RHIC experiments are designed to measure these hadrons (as well as photons and leptons) to provide information about the collision.

2.3 Signals of the Quark-Gluon Plasma

Several different signatures have been proposed to detect the existence of the quark-gluon plasma. The most widely accepted are kinematic probes, strangeness enhancement, J/Ψ suppression, photon production, jet quenching, and event-by-event fluctuations. However, none of these possible signatures are strong enough indicators to prove the existence of the QGP. Several of these signatures will be needed simultaneously to make a sufficient case for its existence.

2.3.1 Kinematic Probes

Thermodynamic properties can be extracted from the collision observables. The temperature T, entropy density s, and energy density ε, are identified with the average transverse momentum $\langle p_t \rangle$, the hadron rapidity distribution dN/dy, and the transverse energy dE_t/dy respectively [Har96]. A first order QGP phase transition is revealed in a plot of T as a function of ε. Such a plot would yield a rise, a plateau and a second rise, due to the saturation of T during the mixed phase (similar to Fig. 2.3). However, the measured momentum distribution of hadrons does not reflect the conditions at early stages of the collision, and is often influenced by a collective flow of particles superimposed on the thermal distribution.

2.3.2 Strangeness Enhancement

As early as 1982, the production of strange and anti-strange quarks was proposed as a probe to study the QGP [Raf82]. A significant enhancement in the yield of strange (and anti-strange) quarks is predicted if a phase transition to a QGP occurs. Production during a hadronic phase involves relatively high energy thresholds:

$$\pi + N \rightarrow \Lambda + K\,;\; E_{threshold} \approx 530\text{MeV}\,.$$

However, since the QCD predicted phase transition occurs near the strange quark current mass of 150 MeV, $s\bar{s}$ could be formed via gluon fusion:

$$g + g \rightarrow s + \bar{s}\,;\; E_{threshold} \approx 300\text{MeV}\,.$$

We would therefore expect to see more $s\bar{s}$ pairs produced in a QGP.

2.3.3 J/Ψ Suppression

The J/Ψ particle is the bound state of the charm and anti-charm quark ($c\bar{c}$). It has been predicted that its production will be suppressed in a QGP [Mat86], where the $c\bar{c}$ will be separated due to Debye screening of the color charges. The separated charm quarks are more likely to combine with other quarks to form open charm particles rather than the J/Ψ.

2.3.4 Photon Production

Photons, since they only interact electromagnetically, are of special interest in QGP probes [Ste01]. They have the advantage of having a mean free path much larger than the size of the reaction volume, which means that the photons can provide a direct probe of the initial stages of the collision. Photon emission may be divided into two groups, prompt and thermal. The prompt photons are produced in the hard parton scatterings; the thermal photons are produced during the possible QGP phase and the hadron phase. If a quark-gluon plasma is produced an increase in thermal photons is expected.

2.3.5 Jet Quenching

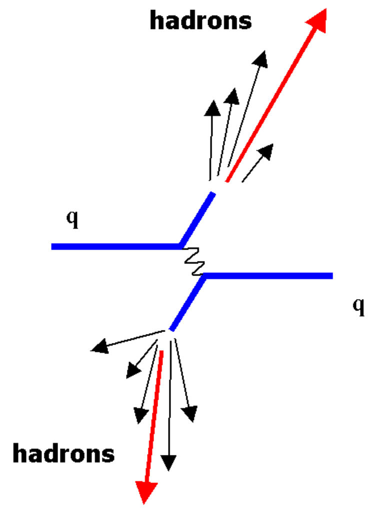

Figure 2.5 Hard scattering of a quark leading to the production of many hadrons in back-to-back cones.

QGP can be probed by its effect on fast partons created during hard parton scatterings. In a process analogous to electromagnetic energy loss of a fast charged particle in normal matter, quark-gluon plasma should have a greater stopping power than normal matter [Gyu94]. This effect is called jet quenching. Jets of particles are created when two partons undergo a hard scattering (see Fig. 2.5). A comparison of the transverse momentum spectrum of hadrons to distributions from pp (or $p\bar{p}$) would show a suppression at high-p_t. Another effect of jet quenching is the disappearance of back-to-back jets [Adl03b]. A parton jet propagating through a dense medium will not only lose energy, it will also be deflected. An analysis can be performed looking for the angular correlations of high-p_t particle jets, looking for a “sudden” disappearance of back-to-back jets.

2.3.6 Event-by-Event Fluctuations

Phase transitions are usually associated with large fluctuations in the vicinity of the critical point. The phase transition from the QGP to the hadron gas might yield nonstatistical fluctuations in particle multiplicities, ratios, and transverse momenta. These fluctuations may be detectable in the final state observables on an event-by-event basis [Ada03c]. RHIC (as well as LHC) has a high enough particle multiplicity to provide the statistics required for this type of event-by-event analysis.

Since quarks carry only fractional charge ($\pm \frac{1}{3}$ or $\pm \frac{2}{3}$ unit charge), the distribution of electric charge in a QGP may be spread more evenly than in ordinary hadronic matter. It is possible that this may survive the phase transition back to hadronic matter. An analysis of the net charge fluctuations on an event-by-event basis can be performed to look for this effect.

2.4 Kaon Production

There are two primary production channels for charged kaons in high-energy collisions, associated production:

$$NN \to N\Lambda K^{+}$$

and pair production:

$$NN \to K^{+}K^{-} + NN\,,$$

where:

N is one of the incoming nucleons, either a proton or neutron.

Strange quarks, s and $\bar{s}$, are thermally produced in equal abundance. Due to the initial conditions in heavy ion collisions, non-strange quarks will be more abundant than non-strange anti-quarks. For the $\bar{s}$ quarks, this permits the formation of $K^{+} = u\bar{s}$, $K^{0} = d\bar{s}$, and $\phi = s\bar{s}$, while the s quarks see an increase in the formation of hyperons (baryons that contain a strange quark, e.g. $\Lambda = uds$). The creation of $K^{-} = \bar{u}s$, $K^{0} = \bar{d}s$, and $\overline{\Lambda} = \overline{u}\overline{d}\overline{s}$ will be less likely, due to the lack of anti-quarks. The K^{-}/K^{+} ratio would be less than 1 in this scenario. However, as the collision energy increases the ratio of $q/\overline{q}$ will approach unity. This would increase the creation of the $K^{-} = \overline{u}s$ to the level of the $K^{+} = u\overline{s}$, and as a result the K^{-}/K^{+} ratio would approach 1.

Section 3

3.1 The Relativistic Heavy Ion Collider

The Relativistic Heavy Ion Collider (RHIC) at Brookhaven National Laboratory (BNL) is the first hadron accelerator and collider consisting of two independent rings. Construction was begun during 1991 and was completed in 1999, for a total cost of $500 million [Oza91]. RHIC is the world's newest facility for basic research in nuclear physics. It is designed to operate at high collision luminosity over a wide range of beam energies and with particle species ranging from polarized protons to heavy ions.

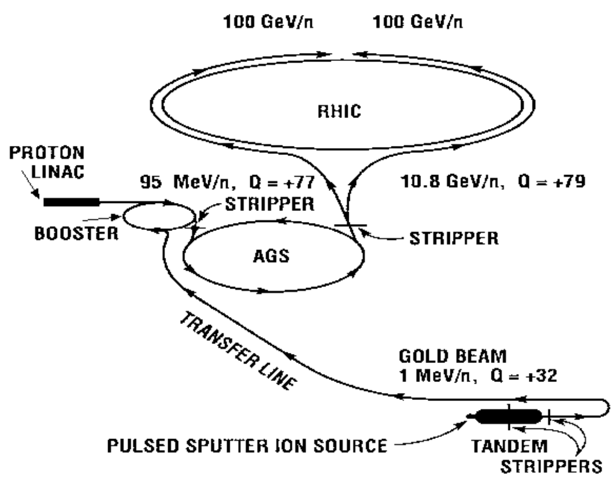

Figure 3.1 Configuration of accelerator complex for RHIC. An accelerator chain, which consists of the Tandem Van de Graaf, the Booster Synchrotron, and the AGS, serves as the injector to the RHIC collider.

3.1.1 Accelerator Complex

The RHIC accelerator complex (Fig. 3.1) is made up of the RHIC rings, the Alternating Gradient Synchrotron (AGS), the Booster Synchrotron, and the Tandem Van de Graaff (TVDG). Gold (Au) atoms are produced in the Pulsed Sputter Ion Source in the TVDG. The positively charged gold ions are accelerated to 1 MeV/nucleon in the TVDG's two 15 million volt electrostatic accelerators. The ions are passed through thin sheets of gold foil, further ionizing the gold atoms, resulting in a distribution of charge states peaking at +32e. The ions enter the Heavy Ion Transfer Line (HITL) where they travel from the TVDG to the Booster

Synchrotron. The Booster Synchrotron accelerates the ions to 95 MeV per nucleon (MeV/n), strips them to +77e, and injects them into the Alternating Gradient Synchrotron (AGS). The AGS increases the energy of the gold ions to 10.8 GeV/n and focuses the ion beam both horizontally and vertically; creating ion "bunches". These bunches are stripped of their remaining electrons (+79e) and transferred to the RHIC via the AGS to RHIC (ATR) transfer line. At the end of this line a switching magnet directs each bunch into either the clockwise (blue) RHIC ring or the counter-clockwise (yellow) ring. The counter rotating beams are accelerated to the desired energy and are stored as circulating beams until they are collided in one, or more, of six (currently only four are occupied) interaction points. Proton acceleration proceeds by a similar path; however, the protons are provided by the Linear Accelerator (LINAC) and injected directly into the Booster Synchrotron.

3.1.2 RHIC Operations

The above process is repeated several times to establish 57 bunches for each ring. The bunches are captured in stationary buckets of the acceleration R.F. system operating at ~26 MHz. When the operating beam energy is reached, the bunches are transferred to the storage R.F. at ~160 MHz. This, six times higher, frequency was chosen to compress the stored bunch so that a short collision diamond can be obtained for head-on collisions, an advantage for experiments.

The top kinetic energy of each beam is designed to be 100 GeV/n for heavy ions, about 125 GeV/n for light ions, and 250 GeV for protons. The collider is able to operate over a wide range of energy, typically from 20 GeV/n to the top energy.

The collider is designed for an Au-Au luminosity of about $2\times10^{26}cm^{-2}s^{-1}$ and a proton-proton (p-p) luminosity of $1.4\times10^{31}cm^{-2}s^{-1}$ at the top energies [Oza91]. The luminosity will be higher for light ions and is energy dependent, decreasing in first approximation with the beam energy.

The collider can accommodate a range of ion species with mass number of about 1 to 200. Asymmetric operation with protons colliding with heavy ions is unique to RHIC. Uranium is a viable species and can be considered as a future upgrade but requires the development of a suitable ion source.

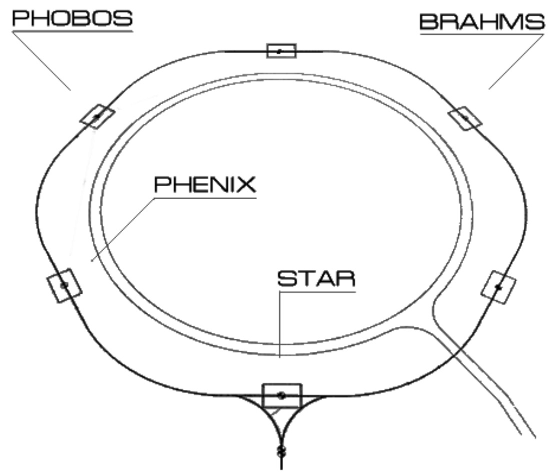

Figure 3.2 Location of the four experimental detectors at RHIC. Two of the six beam interaction regions are not currently in use.

The luminosity lifetime is about 10 hours for Au-Au operation at the top energy. The drop in luminosity over the 10-hour store is due to intra-beam scattering, which causes emittance growth. An upgrade of the RHIC luminosity by a factor of four can be achieved by doubling the number of bunches to about 120 and by increasing focusing at the interaction regions [Ros02].

3.1.3 RHIC Experiments

RHIC's 3.8 km rings have six interaction points where the two beams collide (Fig. 3.2). These collisions provide physicists working at the experimental detectors with information about fundamental nuclear phenomena. There are currently four experiments operating at RHIC, two small ("table top") and two large experiments (both in size and collaboration).

The PHOBOS concept is based on the premise that interesting collisions will be rare but that when they do occur the new physics will be readily identified. Thus the PHOBOS detector is designed to be able to examine and analyze a very large number of unselected gold-gold collisions. For each collision the detector gives a global picture of the collision and detailed information about a small subset of the nuclear fragments ejected from the high energy density region. The PHOBOS detector will be able to measure quantities such as the temperature, size, and density of the fireball produced in the collision. It will also study the ratios of the various particles produced. With this information it should be possible to both detect and study a phase transition that might occur between QGP and ordinary nuclear matter.

The **B**road **Ra**nge **H**adron **M**agnetic **S**pectrometers Experiment at RHIC (BRAHMS) is designed to measure charged hadrons over a wide range of rapidity and transverse momentum. One of the physics goals is to study the reaction mechanisms of the relativistic heavy ion reactions at RHIC energies and the properties of the highly excited nuclear matter formed in these reactions. The amount of stopping will be studied through the net baryon distributions. Some information concerning the space-time characteristics of the system will be obtained from interferometry measurements in a limited rapidity and p_t range.

The **P**ioneering **H**igh **E**nergy **N**uclear **I**nteraction E**x**periment (PHENIX) records many different particles emerging from RHIC collisions including: photons, electrons, muons, and hadrons. Photons and leptons are not affected by the strong force, which binds quarks and gluons together into hadrons. These particles can emerge unchanged from the interior of a collision, providing information about processes within the collision.

The fourth detector is the **S**olenoidal **T**racker **a**t **R**HIC (STAR). The data presented in this thesis was taken using the STAR detector. The detector will be described in some detail in the following section.

3.2 The STAR Detector

The STAR detector, by virtue of its large acceptance, specializes in tracking the thousands of particles produced by each ion collision at RHIC. Weighing 1,200 tons and as large as a house, STAR is a massive detector. It is used to search for signatures of the quark-gluon plasma. It is also used to investigate the behavior of matter at high energy densities by making measurements over a large area.

3.2.1 Time Projection Chamber

The Time Projection Chamber (TPC) is the primary tracking detector in STAR. The TPC has an active volume that covers a pseudo-rapidity range of $|\eta| \leq 1.8$ with full azimuthal coverage [Ack03a]. The TPC sits inside a large solenoidal magnet designed with a uniform maximum field of 0.5 T. Figure 3.3 shows a schematic view of the TPC. The TPC is 4.2 m long and 4 m in diameter. It consists of a large volume of P10 gas (90% argon, 10% methane) in a well-defined uniform electric field of ~135 V/cm [And03]. The paths of primary ionizing particles passing through the gas volume are reconstructed with high precision from the released secondary electrons that drift to the readout end caps at the ends of the chamber. The uniform electric field required to drift the electrons is defined by a thin, conductive central membrane at the center of the TPC.

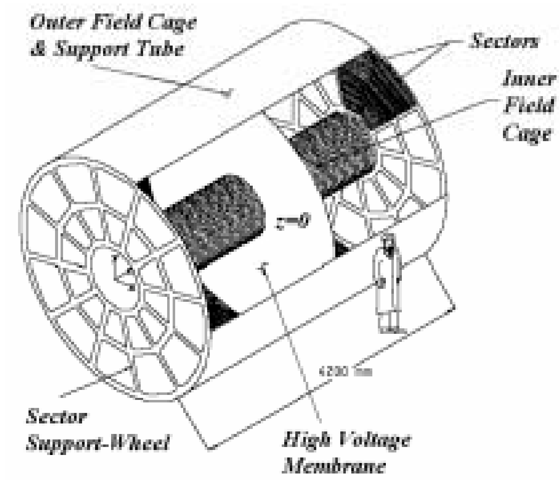

Figure 3.3 Schematic view of the STAR TPC. The collisions take place near the center of the TPC (*z=0*).

The readout system is based on a Multi-Wire Proportional Chamber (MWPC). The drifting secondary electrons avalanche in the high fields at the anode wires providing amplification of 1000 to 3000. The positive ions created in the avalanche induce a temporary charge on the pads which is measured by a preamplifier/shaper/waveform digitizer system. The induced charge from an avalanche is shared over several adjacent pads, so the original track position can be reconstructed to a small fraction of a pad width. There are a total of 136,608 pads in the readout system.

3.2.2 Other STAR Detectors

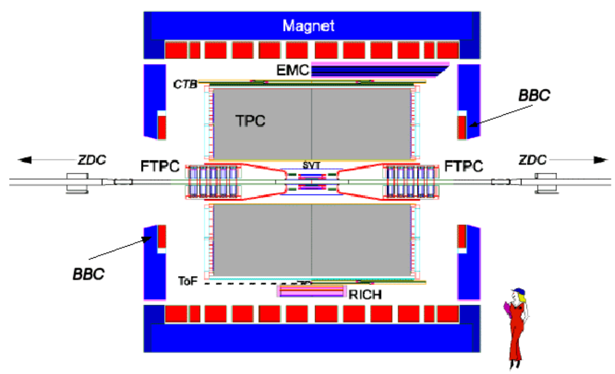

Figure 3.4 Cutaway view of STAR detector showing the location of all the detectors. The TPC was the primary tracking detector used in this analysis.

STAR consists of several detectors besides the TPC (Fig. 3.4). These detectors range from calorimeters, measuring particle energies, to silicon detectors, for improved tracking. These detectors greatly extend the capabilities of STAR to detect and identify high energy and rare short-lived particles.

The detector closest to the primary collision is the Silicon Vertex Tracker (SVT). SVT tracking close to the interaction allows precision localization of the primary vertex, as well as identification of secondary vertices from weak decays, e.g. Λ, Ξ, and Ω. The SVT consists of 216 silicon drift detectors (equivalent to a total of 13 million pixels) arranged in three cylindrical layers at distances of approximately 7, 11, and 15 cm from the beam axis. The SVT covers a pseudo-rapidity range $|\eta| \leq 1$ with complete azimuthal symmetry $\Delta\phi = 2\pi$ [Bel03].

The Forward Time Projection Chamber (FTPC) was designed to extend STAR's tracking in the forward region, $2.5 < |\eta| < 4.0$. It consists of two identical chambers located within the TPC inner field cage, close to the beam pipe at ±1.5 m from the center of the TPC (defined as $z = 0$). The FTPC has a cylindrical structure, 75 cm in diameter and 120 cm long. The FTPC is similar to the STAR TPC, with the exception that the drift direction of the electrons is radial as opposed to axial, with respect to the beam axis. This radial drift configuration was chosen in order to optimize the two-track separation in the region close to the beam pipe where the particle density is highest [Ack03b].

The Ring Imaging Cherenkov (RICH) detector extends the particle identification capabilities for charged hadrons in STAR at mid-rapidity, $|\eta| < 0.3$. The RICH detector consists of a liquid radiator and a photodetector. A particle that enters the radiator traveling faster than the speed of light, in the given medium, will emit Cherenkov radiation. The Cherenkov radiation is not emitted isotropically, but with a definite polar angle with respect to the particle velocity. The projection of this Cherenkov light cone onto a plane will produce a ring whose diameter is directly related to the particle's velocity. Using the momentum of the track from the TPC, along with the velocity allows the calculation of the particle's mass [Bra03].

The Zero Degree Calorimeters (ZDCs) were designed to detect neutral beam fragments downstream of RHIC collisions at very small angles ($\theta \le 4mr$). Two detectors are located at each experiment, ~18m downstream from the interaction point ($z = 0$), in order to more easily compare RHIC results. A coincidence of the two beam directions defines a minimum bias selection of heavy ion collisions. The ZDCs are hadronic calorimeters using layers of tungsten absorbers together with Cherenkov fibers. Light generated in the fibers is directed to three photo-multiplier tubes (PMT) [Adl01a].

The Central Trigger Barrel (CTB) was also designed to be part of the trigger system for the STAR detector. The CTB is made up of 240 scintillator slats placed around the exterior of the TPC, resulting in a pseudo-rapidity coverage of $-1 < \eta < 1$. Each scintillator slat is 1 cm thick by 21 cm wide. The CTB signal is correlated to the multiplicity at mid-rapidity, and was used as part of the central trigger.

The Beam-Beam Counter (BBC) was designed to provide a trigger for the pp data running. It will also be able to suppress unwanted beam-gas events. There are two BBCs located near the beam pipe, mounted on the East and West magnet pole tip. Each counter consists of two rings of hexagonal scintillator tiles: an outer ring composed of 18 large tiles and an inner ring composed of 18 small tiles. The timing difference between the two BBC counters will also be able to locate the position of the primary vertex. Only 1/3 of the detector was installed for the pp running.

3.2.3 STAR Beam Pipe

The beam pipe at the STAR interaction region was designed to reduce the number of secondary particles hitting the SVT and TPC. The Stainless Steel beam pipe of the RHIC accelerator transitions to aluminum near the detector (at $z = \pm 402.59cm$) [Mat03]. As the beam pipe nears the center of the detector, it transitions from aluminum to beryllium (at $z = \pm 76.20cm$) [Mat03]. The aluminum section is a compromise since it has a higher background rate than the beryllium pipe; however, it is easier and safer to handle and is much cheaper.

Section 4

4.1 TPC Reconstruction

This section will discuss the offline event reconstruction process required to convert raw data into reconstructed tracks. After a collision has occurred in the STAR detector, the trigger decides whether or not to accept the data from the various detectors. If accepted, this data is read and recorded by the **D**ata **Acq**uisition system (DAQ) [Lan03]. It is stored for later reconstruction at the **H**igh **P**erformance **S**torage **S**ystem (HPSS) at BNL.

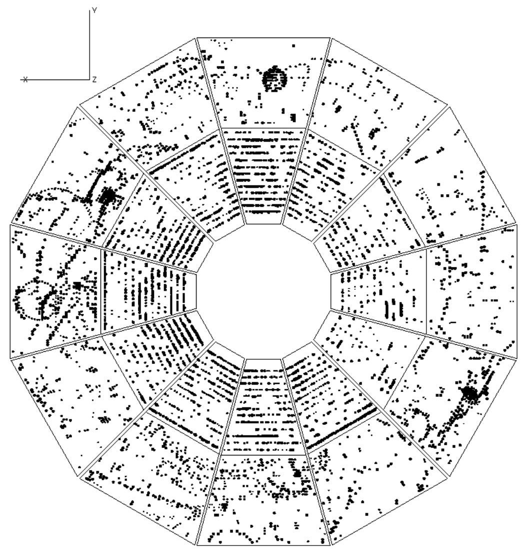

Figure 4.1 A TPC event prior to tracking. Each dot is a hit recorded by the TPC pad plane.

The event reconstruction chain includes detector specific software for reconstruction and calibration for each detector operating during the run. However, since all data presented in this thesis comes from the TPC, I will focus on reconstruction in this detector.

4.1.1 Cluster Finding

Figure 4.1 shows a typical TPC event. Each point represents a charge cluster (often referred to as a hit) recorded by the TPC pad plane. Hits are created when a charged particle travels through the TPC ionizing gas along its track. These ionized electrons drift along the electric field and are recorded by the pad planes. Each sector

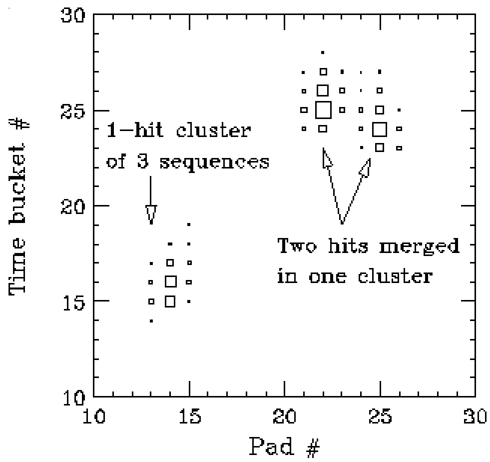

Figure 4.2 Pixel data for part of a pad row is shown for three tracks crossing the row. The size of a box indicates the magnitude of the ADC value of the pixel [Lis96].

contains 5692 pads (1750 inner sub-sector and 3942 outer sub-sector) which are each sampled 512 times (maximum, 380 typical), resulting in ~70 million total ADC values [Lis96].

The first task of the reconstruction software is to convert the raw pixel data into space points. The clusters are found separately in *x*, *y*, and *z* space. The local *x*-axis is defined to be along the direction of the pad row; the local *y*-axis is perpendicular to the pad row extending toward the beam line; the *z*-axis lies along the beam line. The *x* position cluster finder looks for ionization on adjacent pads within a pad row, having similar drift times. The *y* position cluster finder looks for ionization on adjacent pads rows with similar drift times, and the *z* position cluster finder looks for ionization in adjacent time bins (also called time buckets) on the same pad. For simple clusters, the energy from all pads is summed to give the total ionization for the cluster. A complex cluster can occur if tracks become too close to resolve (see Fig. 4.2). An algorithm is applied that looks for two peaks divided by a valley. A cluster is assigned the *x-y* coordinates of each peak, and the ionization is divided evenly between them. These merged clusters can only be used for tracking. Merged clusters cannot be used for dE/dx calculations since the ionization cannot be properly assigned to a specific cluster. Complex clusters occur in about 30% of all clusters in a central AuAu event [Lis96].

Once the charge clusters have been found, they are transformed into TPC space points by calculating their global *x-y* from their local *x-y*, and their *z*-coordinate from the drift velocity. The space points then contain information about the hits in the STAR global coordinates and the energy deposited by the particle.

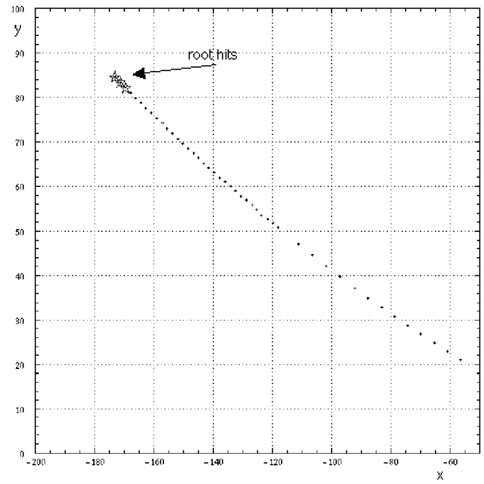

Figure 4.3 Hypothetical high p_t track in the TPC. Dots are space points (hits); the stars are the roots of the track [Sak94].

4.1.2 Track Finding

The environment in which the STAR detector operates is unlike anything previously seen in other colliders or fixed target experiments. The largest problems are the high track density (~3000 tracks per event in central AuAu collisions) and the low average momentum of the produced particles [Boc90]. The latter problem can disturb the topology of the event through multiple scattering and energy loss. Tracking software designed for the ALEPH TPC [Atw91]and modified for the higher track density of NA36 [Gar89] was used as a model for STAR software [Sak94].

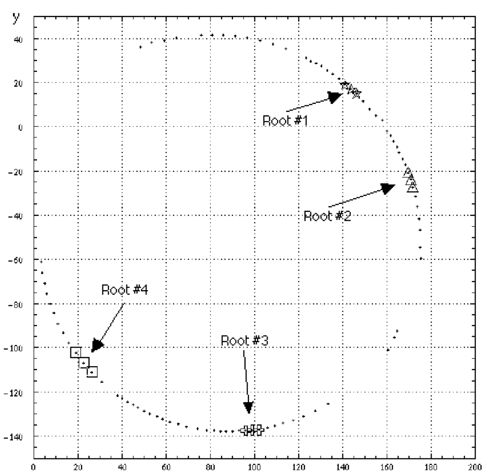

Figure 4.4 Hypothetical low p_t track in the TPC. Dots are space points (hits); the stars are the roots of the track. The tracking algorithm finds four roots for this track [Sak94].

In order to describe the operation of the STAR tracking software (tpt), this section will follow the tracking procedure for two hypothetical tracks (Fig. 4.3 and 4.4). The first track will have a transverse momentum (p_t) of 1GeV/c and the second will have a p_t of 150 MeV/c (barely entering the TPC at full magnetic field).

The first step to find a track in the TPC is root finding. The tracking program looks for a set of three-point links, which form a line segment. The search is performed starting from the outer most pad row, since the multiplicity will be lowest, working toward the inner pad rows. For the 1 GeV/c track, the roots are simply the outer most three points (Fig. 4.3), however the problem is more complicated for the low p_t track. Since this track does not pass the root finding cuts in the outer row, the program moves inward until the cuts are satisfied. This results in the tracking algorithm finding four separate roots for this track (Fig. 4.4).

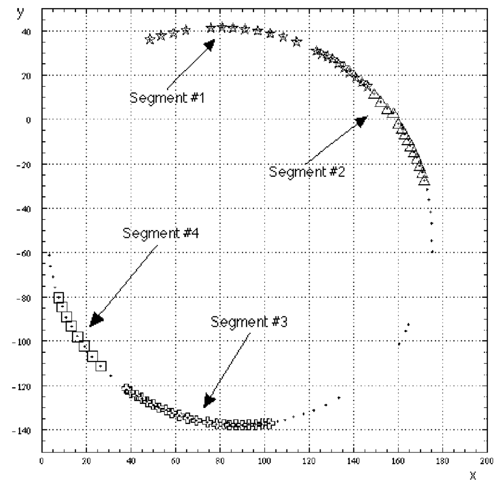

Figure 4.5 The results of the segment formation in the tracking algorithm. The symbols represent the different segments formed from the four roots. The dots are space points that have not been associated with any segments.

Immediately after finding a root, the tracking software begins looking for track segments. The segment formation step successfully associates all 45 possible hits to the 1 GeV/c track. Track reconstruction is now complete for the 1 GeV/c track. Since four roots were found for the 150 GeV/c track, four segments were formed (Fig. 4.5). There are still several points that have not been associated with a segment. This is due to the fact that the segment formation process only extends roots inward.

The next step, segment extension, is needed to include the remaining points. The segment extension phase of the tracking algorithm uses a helix model projected both inward and outwards from the segment to include any points that lie within tolerances of the projection. Virtually all points are now included in one of the four segments.

The final step is to search for segments that belong to the same track. This step is handled by the helix-merging portion of the tracking algorithm. The helix parameters are obtained from helix fits to the segments. If the parameters agree within tolerances, the segments are merged into a single track segment. The result is that an optimized helix merging routine would merge all four of our 150 MeV/c segments into one final track.

4.1.3 Event Vertex

The next task in the reconstruction is finding the collision vertex for the event. An accurate vertex determination is required for two main reasons. First, it can be used to re-calculate the momentum vector for each primary particle (particles that originate from the collision) by including the vertex as a point on the track. Second, it is necessary in determining whether a particle is a primary track or a secondary track (tracks resulting from decays of primary particles, interactions with detector materials, etc...).

The vertex reconstruction employs a Least Squares Method (LSM), as well as a simple technique for removing outlier tracks [Ceb92]. To begin a track is extrapolated back to an initial reference point. At RHIC, this reference point is in the transverse plane, since the probable interaction point is known much better in this plane then in the *z*-axis ($\sigma_{trans} \approx 0.5mm$, $\sigma_{z-axis} \approx 90cm$). The distance of closest approach, d_i, is calculated for each track, i, from some reference space point along the beam axis. The sum is calculated, $\chi^2 = \sum d_i^2$, and minimized to obtain an estimate for the primary vertex [Boc90]. Secondary particle tracks can extrapolate far from the primary vertex, significantly effecting the estimated vertex position. A simple truncation method is used to remove these outliers improving the fit. This process is repeated several times, using the calculated vertex as the seed vertex for the next iteration. A stable result is usually obtained after 3-4 iterations.

This method of finding the vertex is best applied to large multiplicity events (>20 tracks). The accuracy for events having a large number of tracks is $\approx 150\mu m$ in both the transverse and beam directions. The efficiency for events having greater than 50 primary tracks is near 100% [And03].

4.1.4 Primary Track Fitting

Once the primary vertex has been reconstructed, global tracks that extrapolate to within 3cm of this point are chosen as primary tracks. Primary tracks are then refit using the vertex as an additional space point. In high multiplicity events, the error associated with the primary vertex is much smaller ($\sim 150\mu m$) than the error in the reconstructed TPC space points ($\sim 700\mu m$). This allows a significant improvement in the tracks momentum resolution.

The path of a charged particle in a static uniform magnetic field can be described using a helix with an axis along the field lines. The parameterization below describes the helix in Cartesian coordinates as a function of path length *s* [Sak94]:

$$x(s) = x_0 + R_H\left[\cos\left(\Phi_0 + \frac{h \cdot s \cdot \cos\lambda}{R_H}\right) - \cos\Phi_0\right]$$

$$y(s) = y_0 + R_H\left[\sin\left(\Phi_0 + \frac{h \cdot s \cdot \cos\lambda}{R_H}\right) - \sin\Phi_0\right]$$

$$z(s) = z_0 + s \cdot \sin\lambda$$

where:

s is the path length along the helix

x_0, y_0, z_0, are the coordinates of the starting point of the helix ($s = s_0 = 0$)

λ is the slope of the helix, also referred to as the dip angle

R_H is the radius of the helix. It can be calculated by:

$$R_H = {P \cdot \cos\lambda}/{|q \cdot B \cdot \kappa|} = 1 \Big/ \left(1/p_t \right) \times 0.001499$$

assuming the standard STAR magnetic field.

κ is a conversion factor (if radius is in centimeters, magnetic field is in kilogauss and momentum is in GeV/c, then $\kappa = 0.00003$)

B is the value of the magnetic field

q is the charge of the particle

h is the sense of rotation of the projected helix in the x-y plane

z is the polar axis parallel to the helix axis

Φ_0 is the azimuthal angle of the starting point of the helix in cylindrical coordinates with respect to the helix axis

This parameterization allows us to calculate useful experimental quantities such as:

$$p_t = R_H \times |qB\kappa|,$$

$$P_z = p_t \tan\lambda,$$

and $p = \sqrt{p_t^2 + p_z^2}$.

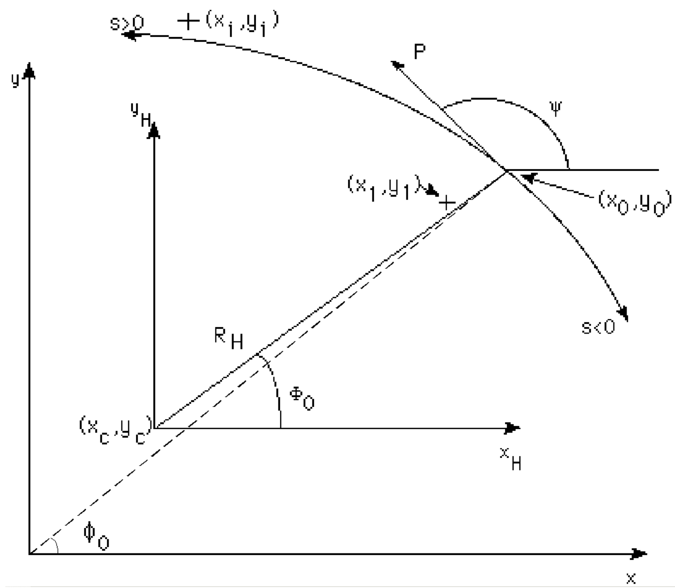

Figure 4.6 Projection of the helix on the x-y plane. (x_i, y_i) are the points on the track [Sak94].

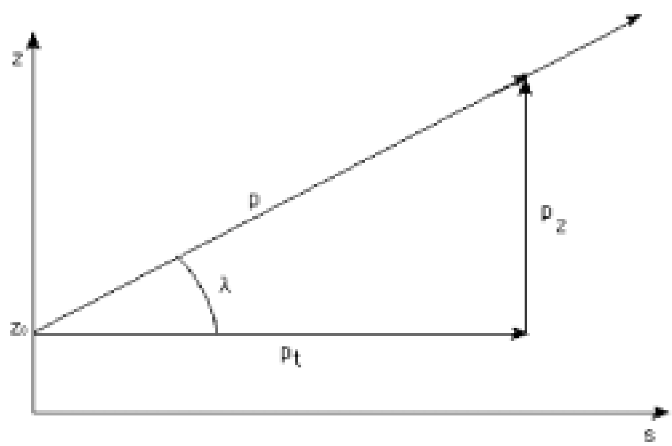

Figure 4.7 Projection of the helix on the s-z plane (bend plane). See above text for symbol descriptions [Sak94].

Figure 4.6 shows the projection of the helix in the *x-y* plane. The momentum vector is shown as a tangent at one of the fit points on the track (x_0, y_0). The global coordinates are shown as well as the coordinates after the rotation into the helix frame of reference. Figure 4.7 is the projection in the *s-z* plane. The helix is a straight line with a momentum *p*. The figure shows the p_t and p_z momentum components.

Section 5

5.1 Particle Identification

Among the oldest and most widely used types of radiation detectors are those based on the ionization created when a charged particle passes through a gas. Heavy charged particles interact with matter primarily through Coulomb forces between their positive charge and the negatively charged orbital electrons of the material. When a charged particle enters a gas, it immediately interacts with many electrons. For any given interaction, the electron feels an impulse from the attractive Coulomb force as the particle passes. Depending on the proximity of the interaction, the electron may be raised to a higher-lying shell within the atom (*excitation*) or it may be removed completely (*ionization*). The energy used to promote or remove the electron must come from the charged particle; its velocity is therefore decreased as a result of the interaction. In particularly strong interactions, the electron may have sufficient kinetic energy to create more ions. Electrons from these secondary interactions are often called delta electrons (Fig. 5.1).

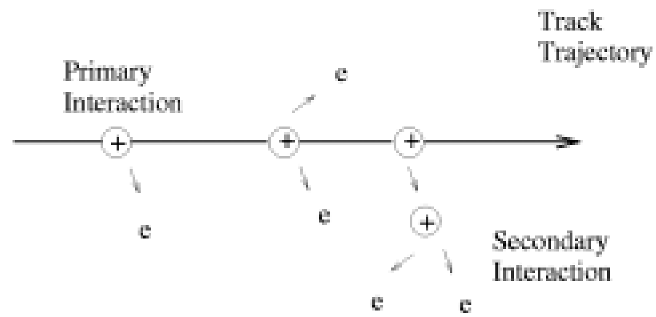

Figure 5.1 Schematic view of a heavy charged particle producing ionization [Las97].

5.1.1 Ionization Distribution

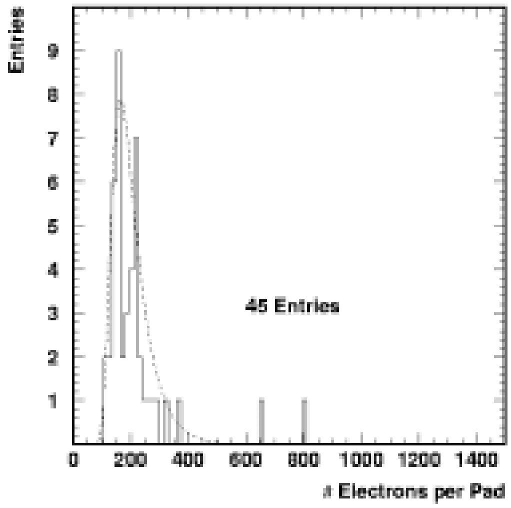

Figure 5.2 Ionization of a track with 45 space points in Ar gas. The dotted line is an approximation to a Landau curve [Las97].

Particle **id**entification (PID) using specific ionization is limited due to the statistical nature of the interactions. Very large fluctuations in the energy transferred are possible over the entire track length. Figure 5.2 shows the number of electrons ionized for a sample track with 45 space points. The distribution resembles a Landau Curve characterized by the long tail.

Next we need to calculate an average or mean value for the tracks energy loss to accurately reflect its velocity. The most straightforward measure, averaging over all n values, would include large fluctuations due to the underlying statistical processes. Two other possibilities are the mean (or arithmetic average) and the most probable (or the maximum of the distribution). For a Landau distribution, the mean is extremely sensitive to the number of counts in the tail. The most probable is a much more reliable quantity [Rol93].

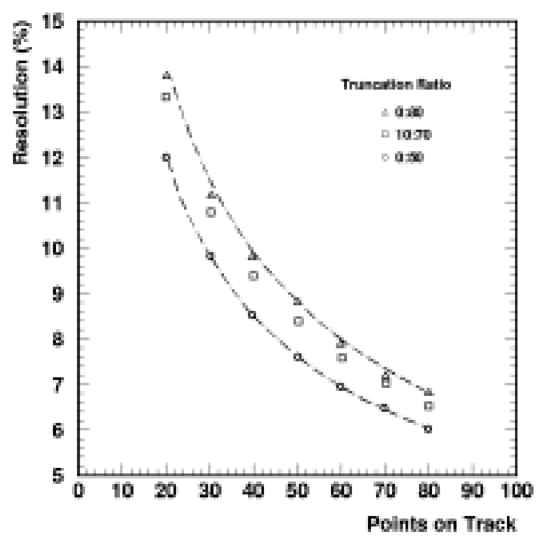

Figure 5.3 Truncation ratio as a function of resolution vs. track points. a:b is the fraction of lowest (a) to highest (b) to be kept for the calculation of the most probable value [Las97].

The most probable value can be calculated by truncating a fixed fraction of the samples in order to create a Gaussian shaped distribution. The mean of this distribution, often referred to as the truncated mean, is the most probable value.

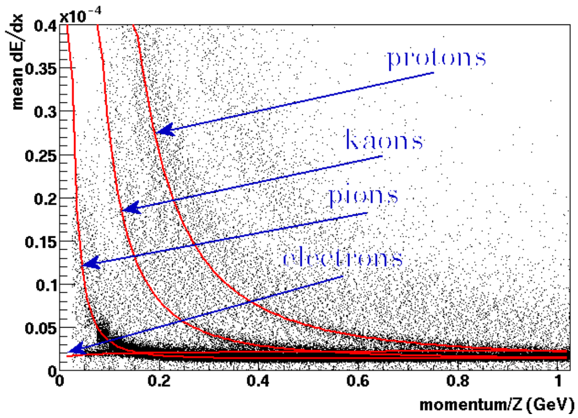

Figure 5.4 Truncated mean dE/dx vs. rigidity. This data is ~14M tracks from STAR, year 2000, AuAu collisions with a 0.25 T magnetic field.

The best truncation ratio is determined experimentally by optimizing the resolution:

$$R = \sigma\left(\frac{dE}{dx}\right) \Big/ \left\langle \frac{dE}{dx} \right\rangle .$$

Figure 5.3 shows the results for several different truncation ratios. A truncation ratio of 0:30, meaning that the lower 70% of the points were used to find the truncated mean, was determined to be optimum.

5.1.2 Bethe-Bloch Relation

Figure 5.4 is a plot of the truncated mean ${dE}/{dx}$ for ~14M tracks vs. the total momentum/charge (${p}/{z}$ or rigidity). We can see good particle separations for each particle species. The lines in the plot are predictions of the energy loss calculated using the Bethe-Bloch formula [Hag02, Kno89]:

$$-\frac{dE}{dx} = Kz^2 \frac{Z}{A} \frac{1}{\beta^2} \left[\frac{1}{2} \ln \frac{2m_e c^2 \beta^2 \gamma^2 T_{\max}}{I^2} - \beta^2 - \frac{\delta}{2} \right]$$

where:

K is defined as $K = 4\pi N_A r_e m_e c^2$ or 0.307075 MeV cm^2.

z is the charge of the incident particle.

Z is the atomic number of the TPC gas.

A is the atomic mass of the TPC gas.

β is defined as $\beta = {}^{v}\!/_{c}$.

γ is defined as $\gamma = {}^{1}\!\big/_{\sqrt{1-\beta^2}}$.

T_{max} is the maximum kinetic energy which can be imparted to a free electron in a single collision.

I is the mean excitation energy of the TPC gas.

δ is the density effect correction to the ionization energy loss.

5.2 Calibration

Several factors, which effect the apparent ionization, must be kept under control. These include the gas density (pressure and temperature), concentration ratios of gas components, electron attachment, baseline and pedestal shift of electronic channels.

5.2.1 Gas Density

The TPC is kept at a constant 2 mbar above atmospheric pressure. This means that the gas pressure varies with time. For the 2001 run, a wire chamber was operational inside the TPC gas return line monitoring the gas gain from an ^{55}Fe source [Kot03]. This signal will be used to calibrate the 2001 data. Since this chamber was not in place for the 2000 run, gas gain was monitored by averaging the signal for tracks over the entire TPC volume. Local gas gain variations were calibrated by calculating the average signal on one row of pads on a single pad-plane and assuming that all pad-rows measure the same signal.

The cooling system is designed to maintain an inlet temperature of 24°C ± 1°C. This is accomplished using a point of use heat exchanger. Four temperature sensors monitor the gas mixture within the TPC. These temperatures are logged in a database.

5.2.2 Gas Concentrations

The gas systems dedicated computer controlled data acquisition system provides constant monitoring of the gas mixture composition via a methane monitor. The mixture ratio is fixed by the mass flow controllers. The instability of the mixture is negligible in comparison to the variations in atmospheric pressure. Since gas mixture and density both affect the drift velocity a single, real-time, measure is used to correct this parameter.

5.2.3 Electron Attachment

As the electrons drift in the TPC, they may be absorbed by the gas creating negative ions. This would make clusters with longer drift times appear to have smaller ionization. The noble gasses, and most organic molecules, can only form stable negative ions in collisions with energies of several electron volts. These energies are not reached in the drift chamber. However, some molecules are capable of attaching electrons at much lower energies. The two main concerns are oxygen in the form of O_2 and H_2O. The gas system maintains the level of these two contaminants to < 25 ppm and < 20 ppm respectively [Kot03].

The remaining correction was calculated using ionization created with a laser projected into the TPC. Thirty-six aluminum strips are attached to each side of the central membrane. Electrons are ejected from the strips when the ultraviolet photons from the laser strike the aluminum. The position of each of the strips is known to high accuracy, so that the electrons can be used for spatial resolution measurements [Leb03].

5.2.4 Baseline and Pedestal Shifts

Uncertainties are also introduced by variations in the readout electronics. These variations are caused by different responses of each readout board and occur between pads and groups of pads. Corrections are calculated by pulsing the anode ground plane and pad plane readout system, assuming the responses will be the same for every pad.

Section 6

6.1 Kaon Analysis

In this section I will describe the analysis performed to obtain the kaon ratio and raw kaon spectra for the 130 AGeV, 200 AGeV Au+Au and 200 GeV pp data sets. I will also present the results from these analyses. The basic analysis can be broken into a few steps:

- Select events
- Select tracks
- Calculate "z" variable to help in identifying kaons
- Fit "z" distributions, using multiple Gaussian, shapes
- Extract particle yields
- Calculate ratio

6.2 Event Selection

Several factors are involved in determining which events should be included in the final analysis. These include variables that depend on the entire event; e.g., trigger setup used and vertex position, and variables that depend on the individual track; e.g., the number of ionization space points and the distance of closest approach to the vertex.

6.2.1 Event Triggering

- **Au+Au**

The events used in this analysis were taken from a minimum bias (minbias) data set. A minbias trigger was selected for the analysis to increase available statistics and enable a comparison between multiple collision centralities. This data set was triggered by requiring a coincidence signal in both ZDCs along with a RHIC beam crossing.

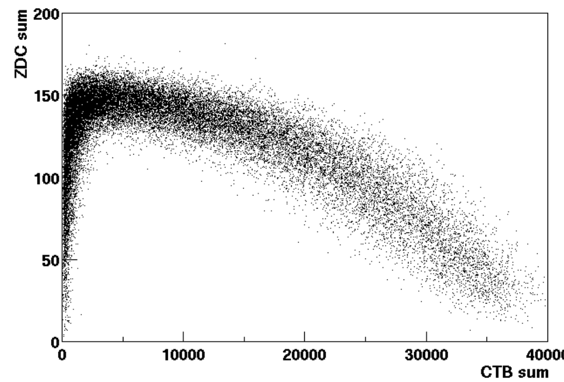

Figure 6.1 CTB signal versus ZDC signal (ZDC east + ZDC west) for Au+Au collisions @ 200GeV. The anti-correlation between the two detectors can be clearly seen over a wide range.

The correlation between the neutron signals seen in the ZDCs (ZDC east + ZDC west) versus the signal in the CTB shows the characteristic "boomerang" shape (Fig. 6.1) [Bie03]. Peripheral events, which have a small geometric overlap, result in a small number of neutrons detected in the ZDCs along with a low CTB signal. As the centrality increases, increasing the geometric overlap, counts in the ZDC and CTB increase. This reflects the increase in dissociated neutrons (from the projectiles) and increasing event multiplicity. As we continue to higher centrality (larger geometric overlap), we reach a point where many of the dissociated neutrons interact within the reaction volume leaving fewer to be detected in the ZDCs. The result is that the CTB signal continues to grow with centrality; while the ZDC signal decreases.

- **pp**

The proton minbias data set was triggered using a coincidence in the Beam-Beam Counter (BBC). The BBC sees ~40% of total pp cross-section [Kir02].

6.2.2 Centrality Definitions

- **Au+Au**

The collision centrality is defined by the impact parameter *b*; the smaller the impact parameter, the more central the collision. However, since the impact parameter cannot be measured experimentally we must rely on an experimental observable that correlates with the impact parameter.

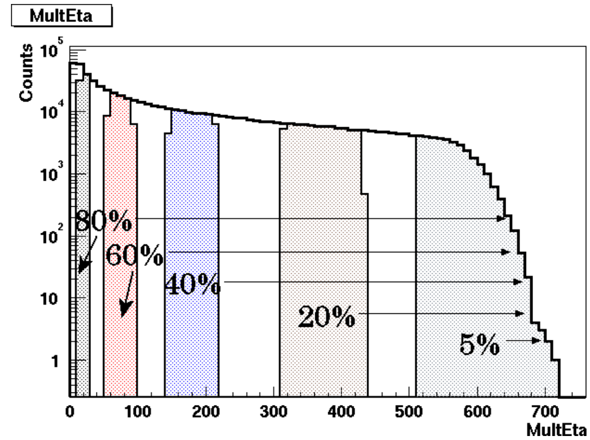

Figure 6.2 Primary track multiplicity distribution for Au+Au collisions @ 200GeV. Only the odd centrality bins are shown for clarity. The cumulative fraction of each bin is shown.

For this analysis, we have chosen the number of negatively charged hadrons. These are particles identified in the TPC, pass within 3 cm of the primary vertex (DCA), and fall within a specified pseudo-rapidity range (for 130 GeV $-0.75 < \eta < 0.75$; and for 200 GeV $-0.5 < \eta < 0.5$). The events are then divided into centrality bins (8 bins for 130 GeV and 9 bins for 200 GeV). Each bin is defined by its percentage of the total multiplicity [Ack01, Adl01b, Cal01]. Figure 6.2 shows the experimental total multiplicity distribution with several centrality bins superimposed. Table 6.1 shows how the centrality bins relate to the number of negative hadrons for 130 and 200 GeV collisions.

Table 6.1 Comparison between number of negative hadrons at 130 and 200 GeV for each centrality bin. The eta range is different for each data set; see text.

Centrality bins	130 GeV	200 GeV
1	23	14
2	48	30
3	76	56
4	106	94
5	141	146
6	182	217
7	216	312
8	256	431
9	-	510

- **pp**

Since proton-proton collisions do not have the same nuclear geometry effects seen in the gold-gold collisions, centrality has less meaning in this context. Each proton is composed of a single nucleon; therefore, pp collisions always consist of the same number of participant nucleons. These collisions produce far fewer charged hadrons, and are not divided into centrality bins. Figure 6.3 is a histogram of the number of charged hadrons for the 200 GeV pp collisions.

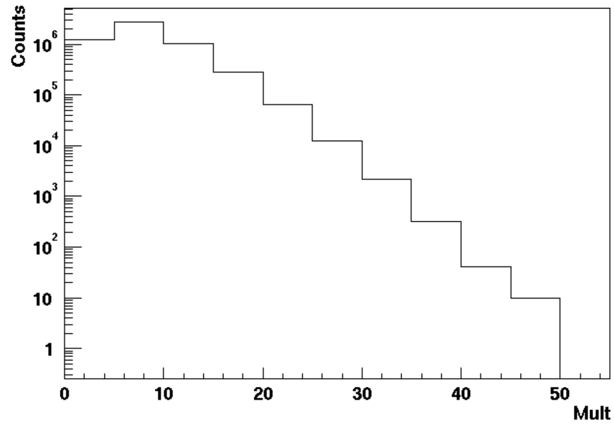

Figure 6.3 Primary track multiplicity distribution for pp collisions @ 200GeV. The pp data is not divided into centrality bins.

6.2.3 Primary Vertex

- **Au+Au**

Collisions took place over a wide range of values along the *z-axis*. However, since the STAR TPC is a symmetric detector we wanted to study mainly those events whose primary vertex was near the center of the TPC ($z = 0$). This would ensure that the average particle would travel the greatest distance inside the TPC. A second consideration during the 200 GeV run, was the position of the support structures for the Silicon Vertex Tracker (SVT), starting at ±25 cm [Wil97]. Events with the primary vertex outside of this range (±25 cm) would see a considerably increased background contribution, due to particles interacting with the support structure. For these reasons, a cut of $|v_z| < 50cm$ was applied to the 130 GeV data and a cut of $|v_z| < 25cm$ was applied to the 200 GeV data.

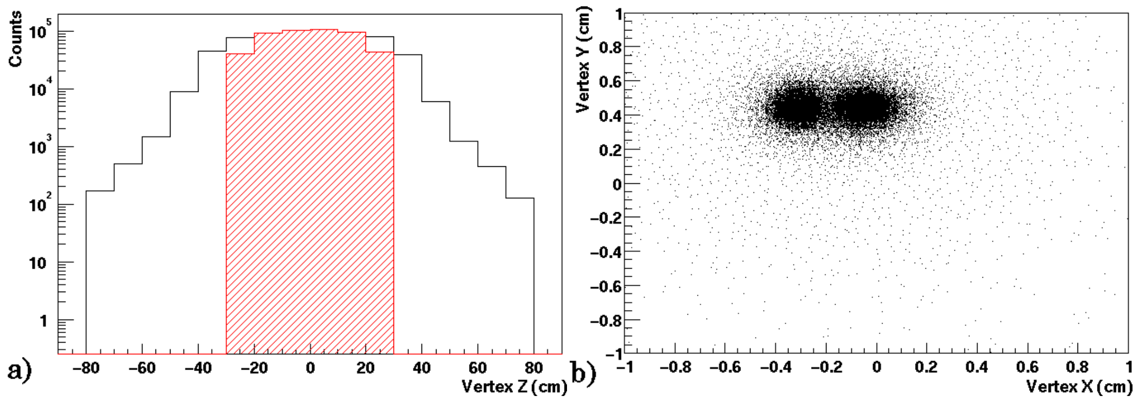

Figure 6.4 Primary vertex distribution for the 200 AGeV Au+Au data set a) along the *z-axis*. Only events with $|v_z| < 75cm$ are kept during initial processing. A cut of $|v_z| < 25cm$ is applied during my analysis. b) in the *x-y plane.* Two beam "spots" can be clearly seen within 1 cm of the TPC center, $(x, y, z) = (0,0,0)$.

Figure 6.4a shows the z vertex cut applied to the 200 GeV data. A previous cut of $|v_z| < 75cm$ was applied during processing. Figure 6.4b shows the position of the collisions in the *x-y plane*. Two "spots" can clearly be seen within 1 cm of the TPC center. A cut of $|v_{x,y}| < 2cm$ was applied for this analysis. The steering of the beam by the RHIC Operations staff, in order to obtain a higher collision rate, most likely causes the two spots seen in Fig. 6.4b.

- **pp**

The pp analysis suffered from the same increased background seen in the Au+Au 200 GeV analysis, due to the increased material of the SVT. Since sufficient statistics were available a cut of $|v_z| > 25cm$ was applied to reduce this background as much as possible.

6.3 Track Selection

The quality of the measured dE/dx depends upon the quality of the individual track. To ensure good tracks, several cuts are applied; however, these cuts, like the event cuts above, trade statistics for quality. The cuts below have been chosen in an attempt to maintain acceptable statistics while increasing the quality of the tracks included in this analysis.

6.3.1 Fit Points

A cut on the number of fit points associated with each track was applied to reduce the number of track fragments included in the analysis. A fit point cut of $FitPts > 15$ was applied to the 130 GeV data. Since the 200 GeV run (Au+Au and pp) had greater statistics, a more stringent cut of $FitPts > 24$ was applied. Figure 6.5 is a histogram of the 200 AGeV Au+ Au data before and after the cut has been applied. This cut removes approximately 27% of the total tracks.

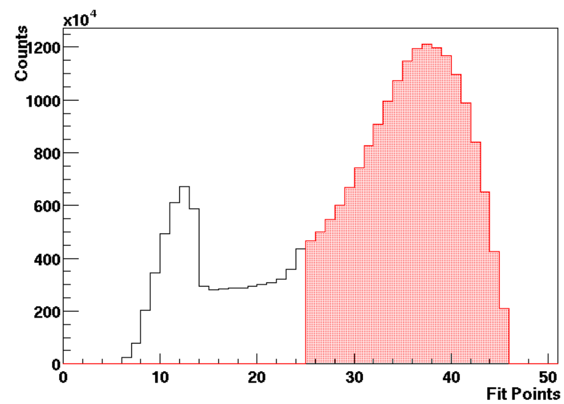

Figure 6.5 Cut on the number of fit points used in the data. Before (black) and after (red) fit points cut for 200 GeV data.

6.3.2 Goodness of Helix Fit

The χ^2 of the helix fits to the track are important to ensure quality tracks are used in the analysis. A cut of $\chi^2 < 3$ per degree of freedom (df) was applied for all data sets. For more information on the helix fitting see section 4.1.4 in this document. Figure 6.6

shows the results of the χ^2 cut on the 200 AGeV Au+Au data. Approximately 5% of the tracks do not pass this cut.

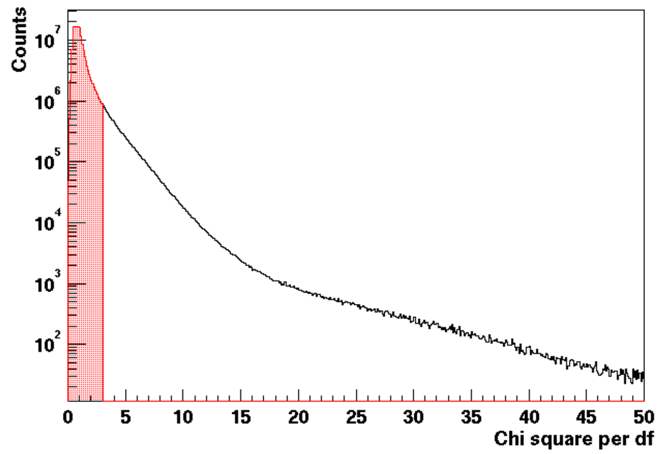

Figure 6.6 Cut on the chi-squared of the helix fit. Before (black) and after (red) the χ^2 cut has been applied to the 200 GeV data.

6.3.3 Fit Points over Max Points

Another cut applied to the data to increase the quality of the tracks is a cut on the ratio of fit points over max points. This cut was set at $\text{FitPoints}/\text{MaxPoints} > 0.55$ for all data sets. This cut can be interpreted as meaning that the track must be using greater than half of its possible fit points in the helix fit. Figure 6.7 shows the results of the fit over max cut on the 200 AGeV Au+Au data. Approximately 12% of the tracks do not pass this cut.

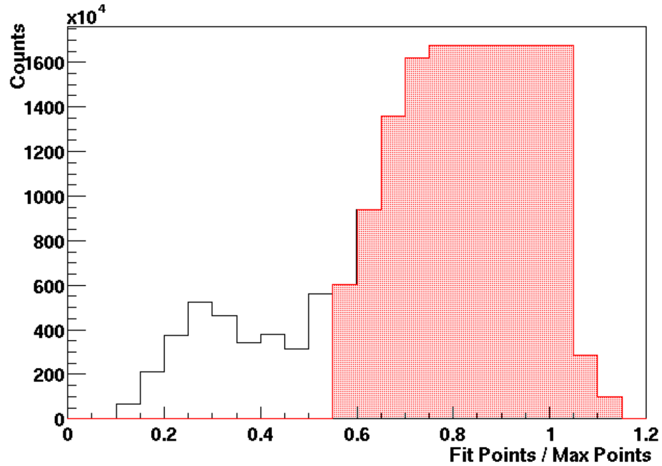

Figure 6.7 Histogram showing the effect of a cut in fit points over the number of maximum points. Before (black) and after (red) the fit over max cut has been applied to the 200 GeV data.

6.3.4 Distance of Closest Approach

The last cut used in this analysis constrains the distance of closest approach (dca) between the track and the event vertex. All primary tracks in the Au+Au collisions (tracks which originate from the collision) are required to pass within 3 cm of the primary vertex, $dca < 3\text{cm}$.

6.4 z – Variable

Particle identification is performed using the dE/dx measurements for each track; however, the TPC does not provide enough power to discriminate between particles on a track-by-track basis. Instead, we use a fitting process over many events. To simplify this fitting process, we divide each track's measured dE/dx by the calculated dE/dx using the Bethe Bloch formula. The logarithm of this value is defined as z:

$$z = \log\left(\frac{dE/dx}{I(i, \vec{p})}\right)$$

where:

$I(i, \bar{p})$ is the predicted ionization for a particle of species i and momentum $\bar{p}$, from the Bethe Bloch formula (see section 5.1.2).

For a pure sample of particle i, this quantity is well described as a Gaussian centered at zero. However for this analysis we have four separate particle species; electrons, pions, kaons, and protons. These particles will be seen as Gaussian shapes offset from zero. Figure 6.8 shows an example of z vs. counts for a typical p_t and rapidity bin.

All of the above data cuts are summarized in table 6.2 for each of the data sets discussed in this thesis. The number of events that passed the cuts is also included in the table.

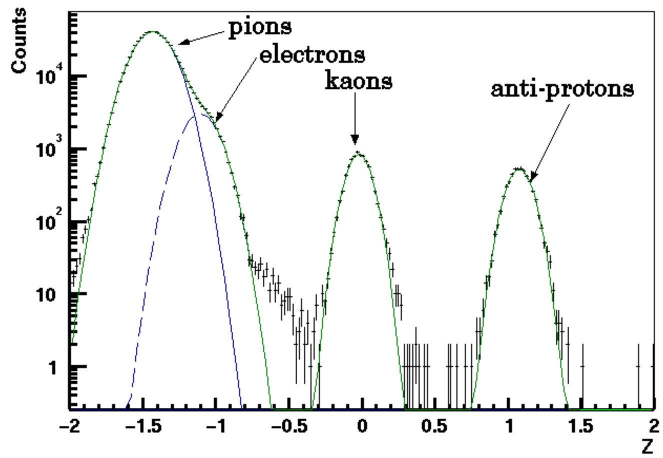

Figure 6.8 A plot of the *z-variable* versus counts for an arbitrary, 50 MeV wide, pt and, 0.1 unit wide, rapidity bin. All four particle-species are labeled. Only the negative particles are shown here. Each peak is fit with a single Gaussian function. The parameters from each individual fit are used to constrain the fit to the entire histogram.

6.4.1 Fitting *z* – Variable

Each centrality bin is further divided into bins of 50 MeV/c and 1 unit of rapidity. To increase statistics and reduce processing time, the positive and negative rapidity bins were combined in the 130 AGeV Au+Au and 200 GeV pp analyses. The ranges for each data set are given in table 6.2.

Table 6.2 Summary of cuts applied to the three different data sets. Refer to the text above for a description of each cut.

Cut	**130 AGeV Au+Au**	**200 AGeV Au+Au**	**200 GeV pp**
Primary vertex	$\lvert v_z \rvert < 50$	$\lvert v_z \rvert < 25$	$\lvert v_z \rvert < 25$
Fit Points	$FitPts > 15$	$FitPts > 24$	$FitPts > 24$
χ^2	$\chi^2 < 3$	$\chi^2 < 3$	$\chi^2 < 3$
Fit/Max	$fom > 0.55$	$fom > 0.55$	$fom > 0.55$
dca	$dca < 3cm$	$dca < 3cm$	$dca < 3cm$
Pt Range (MeV/c)	$150 < p_t < 600$	$200 < p_t < 650$	$200 < p_t < 650$
Rapidity Range	$\lvert y \rvert < 0.4$	$\lvert y \rvert < 0.4$	$\lvert y \rvert < 0.4$
Num. of Events Before Cuts	305,000	650,000	5,400,000
Num. of Events After Cuts	115,000	475,000	2,200,000
K^-/K^+ **ratio**	0.928 ± 0.0028 (stat.)	0.953 ± 0.0012 (stat.)	0.964 ± 0.0039 (stat.)

The z distribution is fit in each of these bins (324 bins for 200 AGeV Au+Au alone) using a Gaussian function:

$$G(x) = \frac{A}{\sqrt{2\pi\sigma^2}} e^{-\frac{(x-\mu)^2}{2\sigma^2}}$$

where:

A is the amplitude,

σ is the standard deviation, and

μ is the mean.

The K^+ and K^- yields and statistical errors are calculated from the Gaussian fits using the following formulas:

$$N_{ij} = A \cdot \sigma \cdot \sqrt{2\pi} \cdot 50 \text{ and } \varepsilon_{ij} = \sqrt{N_{ij}}$$

where:

N_{ij} is the yield from an individual pt and rapidity bin ij,

A and σ are from the Gaussian fit,

50 is a correction due to the histogram bin width, and

ε_{ij} is the statistical error associated with the ij^{th} bin.

6.5 Absorption Correction

Some of the kaons created in the collision will pass through and be absorbed by material located between the TPC active region and the primary vertex. Since the absorption cross-section for the K^- is larger than for the K^+, due to the $\bar{u}$ quark, more K^- are absorbed in the material. If a correction is not made for this effect, than the K^-/K^+ ratio will be artificially low.

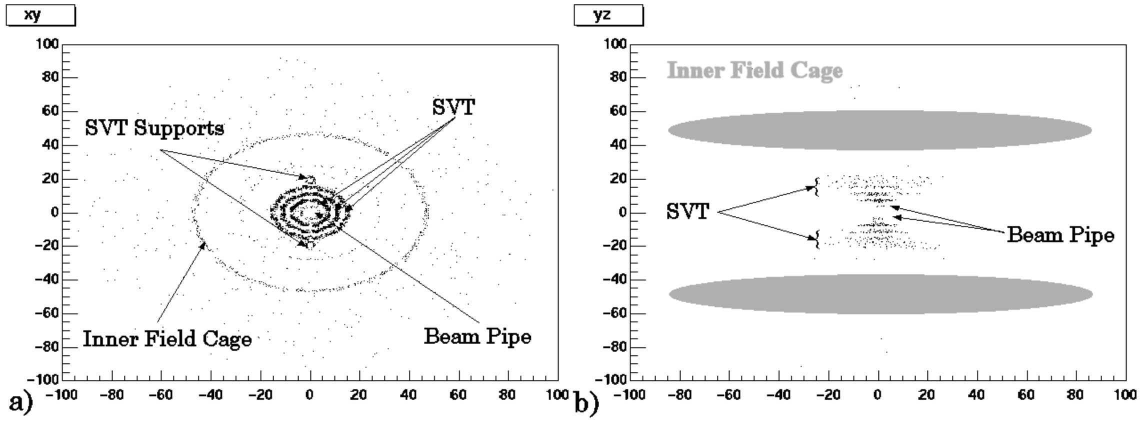

Figure 6.9 Kaon loss in the detector material a) in the *x-y* plane. b) in the *y-z plane.* The SVT structure can be seen near (0,0).

Figure 6.9 shows where the kaons are absorbed in the detector. Figure 6.9a shows an *x-y* slice of the TPC (beam into the page), and Fig. 6.9b shows the *y-z* plane (beam direction parallel to the page). The correction is calculated using the Monte Carlo output (after running through detector simulation) divided by the Monte Carlo input as a function of p_t.

6.6 Electron Contamination

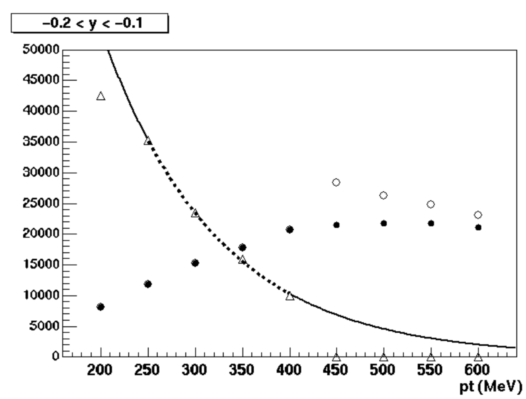

Figure 6.10 Electron contamination extrapolation in the $-0.2 < y < -0.1$ rapidity bin for the 200 AGeV AuAu data. Triangles are electron yield, open circles are kaon yields, closed circles are kaon yield after correction, solid line is exponential fit to the data, and dotted line indicates the fit range (250-400 MeV/c) for this bin.

Figure 5.4 shows the electron band begins crossing the kaon band around 400 MeV/c. At this point, it is impossible to distinguish between kaons and electrons using only energy loss in the TPC. In order to correct for this contamination, we estimate the electron yield and subtract it from the total (electron + kaon) yield.

The electron yield is estimated using the "known" momentum range, where the electrons are separated. This range is fitted using an m_t-exponential function and extrapolated to the overlap region (see Fig. 6.10). The calculated electron yield is subtracted from the contaminated kaon yield resulting in a corrected kaon yield. The 200 MeV/c bin is excluded from the electron fit due to pion contamination.

6.7 Calculating the Ratio and Statistical Error

The K^-/K^+ ratio and error is calculated for each pt and rapidity bin with the following formulas [Bev92]:

$$R_{ij} = \frac{N_{ij}^-}{N_{ij}^+} \text{ and } \varepsilon_{ij} = R_{ij}\sqrt{\left(\frac{1}{\sqrt{N_{ij}^-}}\right)^2 + \left(\frac{1}{\sqrt{N_{ij}^+}}\right)^2}$$

where:

R_{ij} is the ratio for each bin,

i is an individual rapidity bin - e.g. $0.0 < y < 0.1$,

j is an individual p_t bin – e.g. $200 < p_t < 250\text{MeV/c}$, and

ε_{ij} is the error associated with the i,j^{th} ratio.

The next step is to integrate the ratio over a rapidity or pt range, individually using the following formulas:

$$R_i = \frac{\sum_j \frac{R_{ij}}{\varepsilon_{ij}^2}}{\sum_j \frac{1}{\varepsilon_{ij}^2}} \text{ and } \varepsilon_i = \sqrt{\frac{1}{\sum_j \frac{1}{\varepsilon_{ij}^2}}}$$

or

$$R_j = \frac{\sum_i \frac{R_{ij}}{\varepsilon_{ij}^2}}{\sum_i \frac{1}{\varepsilon_{ij}^2}} \text{ and } \varepsilon_j = \sqrt{\frac{1}{\sum_i \frac{1}{\varepsilon_{ij}^2}}} .$$

The result is two sets of ratios, one averaged over rapidity (R_j) and one averaged over p_t (R_i).

The last step is to calculate the final ratio and error. This is done using the same function as above:

$$R = \frac{\sum \frac{R_i}{\varepsilon_i^2}}{\sum \frac{1}{\varepsilon_i^2}} \text{ and } \varepsilon = \sqrt{\frac{1}{\sum \frac{1}{\varepsilon_i^2}}}$$

or

$$R = \frac{\sum \frac{R_j}{\varepsilon_j^2}}{\sum \frac{1}{\varepsilon_j^2}} \text{ and } \varepsilon = \sqrt{\frac{1}{\sum \frac{1}{\varepsilon_j^2}}}$$

These two ratios must be equal, since the order in which the variables are averaged does not affect the result.

6.8 Estimating the Systematic Error

The systematic error for the kaon ratio was estimated by varying the analysis cuts. Table 6.2 shows the cuts used in the full analysis; table 6.3 shows how the cuts were changed for the systematic error analysis.

Table 6.3 Summary of the different cuts applied to the three data sets to estimate the systematic error. Refer to the text in section 6.2 and 6.3 above for descriptions of each cut.

Cut	**130 AGeV Au+Au**	**200 AGeV Au+Au**	**200 GeV pp**
Primary vertex	$10 < \lvert v_z \rvert < 50$	$10 < \lvert v_z \rvert < 50$	$10 < \lvert v_z \rvert < 50$
$\mathbf{p_z}$ *** vtz**	> 0	> 0	> 0
Fit Points	$FitPts > 24$	$FitPts > 29$	$FitPts > 29$
dca	$dca < 3cm$	$dca < 1cm$	$dca < 1cm$
# of Events	38k	268k	1.0M
Systematic error	± 0.03	± 0.01	± 0.01

The primary vertex cut, along with the cut on $p_z * vtz$ (momentum in the beam direction multiplied by the vertex position), excludes any tracks passing through the TPC's central membrane. These cuts were chosen as the most likely to affect event and track quality. The 130 AGeV Au+Au dca cut was not varied due to insufficient statistics. Absorption and electron contamination corrections were not applied to the data.

6.9 Kaon Yield in Au+Au Collisions

The mid-rapidity kaon yields vs. transverse mass extracted from the *z*-variable fits (see section 6.4.1) are plotted in Fig. 6.11. The raw pp yields are also included on Fig. 6.11a. They appear to be consistent with the Au+Au yields. The pp data shown does not include a correction for vertex finding efficiency. This is estimated to be 6-8% and will be considered when the systematic errors are estimated.

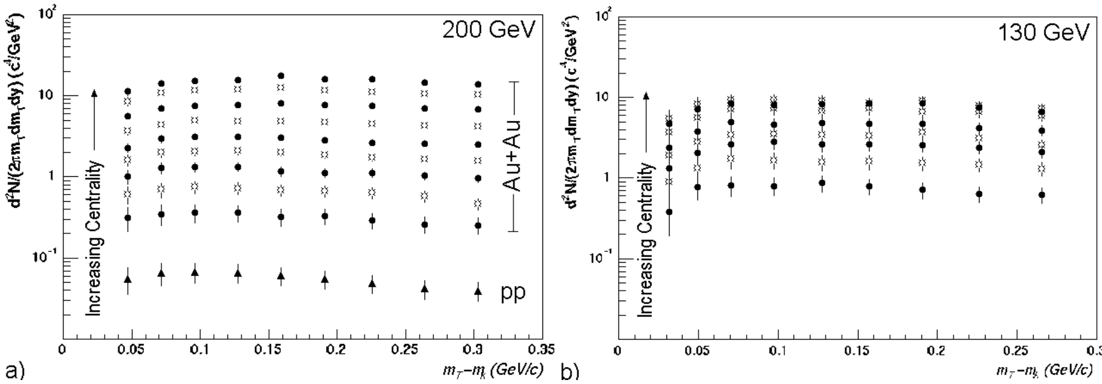

Figure 6.11 Raw K$^-$ yields from 200 AGeV Au+Au and pp data (a) and 130 AGeV Au+Au (b) collision data. K$^+$ distributions (not shown) are very similar to K$^-$. Plots include statistical errors.

The transverse momentum is converted to transverse mass (m_t). This is done to simplify the fit to the corrected data, since it then takes the form of an exponential. The transverse mass is given by:

$$m_t = \sqrt{p_t^2 + m_K^2}$$

where:

m_K is the rest mass of the kaon.

Several corrections must be applied to obtain the corrected kaon spectra.

6.9.1 Electron Contamination

The electron contamination is corrected using the method described in section 6.6. An uncorrelated bin-to-bin systematic error of 15% for the Au+Au data (25% for pp data) has been estimated on the yields in this region.

6.9.2 Absorption, Acceptance, Decay, and Efficiency Corrections

Kaon loss by hadronic interaction (absorption), detector acceptance, decays, and tracking efficiency were corrected using Monte Carlo (MC) embedded data. The embedding procedure takes a real event and inserts MC tracks into the raw data file.

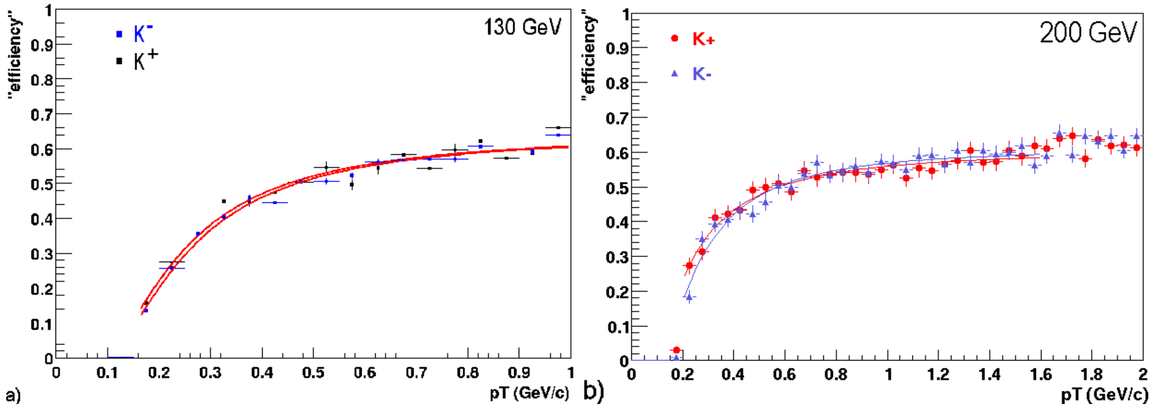

Figure 6.12 Kaon efficiency vs. transverse momentum for 130 GeV (a) and 200 GeV (b). Plots and efficiency corrections provided by A. Cardenas [Car02] and O. Barannikova [Bar03].

The detector response is modeled using a GEANT MC simulation. The standard reconstruction software is used to processes the data. The ratio of the reconstructed tracks to the embedded tracks is the efficiency. Figure 6.12 shows the efficiencies for 130 GeV and 200 GeV kaons.

The efficiencies are fit to an exponential of the form:

$$eff = p_0 \exp\left(-\left(p_1/p_t\right)^{p_2}\right)$$

where:

p_0, p_1, p_2 are fit parameters and

p_t is the transverse momentum.

These functions are used to correct the corresponding spectra.

6.10 Corrected Kaon Yields

Figures 6.13 and 6.14 shows the kaon spectra after all corrections have been applied. For the Au+Au data, a 15% systematic error is included on points affected by electron contamination and a 10% systematic error is included for all other points; for the pp data, a 25% and 20% are estimated for the same areas. The increase in the systematic error from Au+Au to pp is due to the uncorrected vertex efficiency.

The shape of the K^- and K^+ are very similar within each collision system. This is a strong indication that the kaons have a similar interaction cross-section, therefore show the same flow dynamics. This is also a good indication that the production mechanism and freeze-out systematics are comparable for the kaons.

The kaons from the pp data show a similar shape to the peripheral yields from the Au+Au data set. This similarity suggests a similar production mechanism for the pp data and the peripheral Au+Au data.

The spectra are fit with an m_t exponential function:

$$\frac{d^2N}{2\pi m_t dm_t dy} = \frac{dN/dy}{2\pi(T+m)T} \exp\left(-\frac{m_t - m}{T}\right)$$

where:

dN/dy is the integrated rapidity density,

T is the inverse slope parameter,

m_t is the transverse mass, and

m is the mass of the kaon.

Only dN/dy and T are treated as free parameters. The fit results will be presented in the next chapter (see section 7.3).

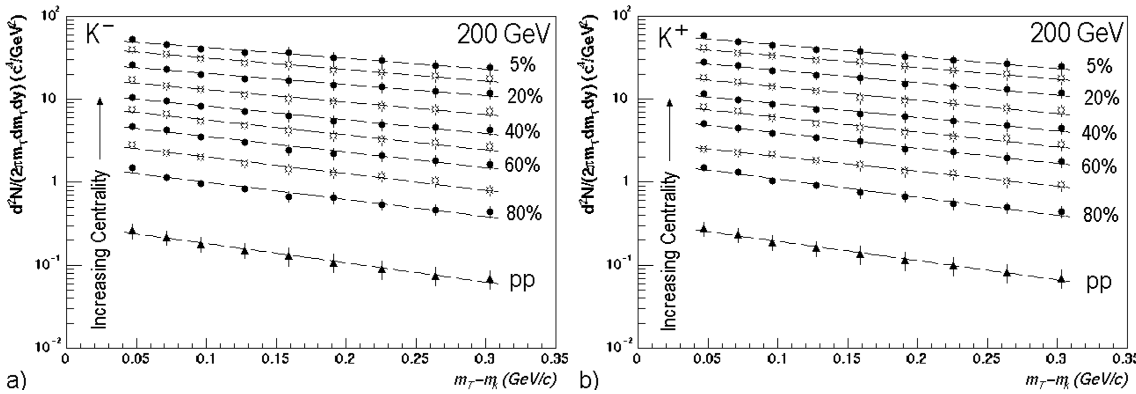

Figure 6.13 Corrected kaon yields from 200 GeV. Every other centrality bin is labeled starting with the top centrality. The results for the 200 GeV pp is also included.

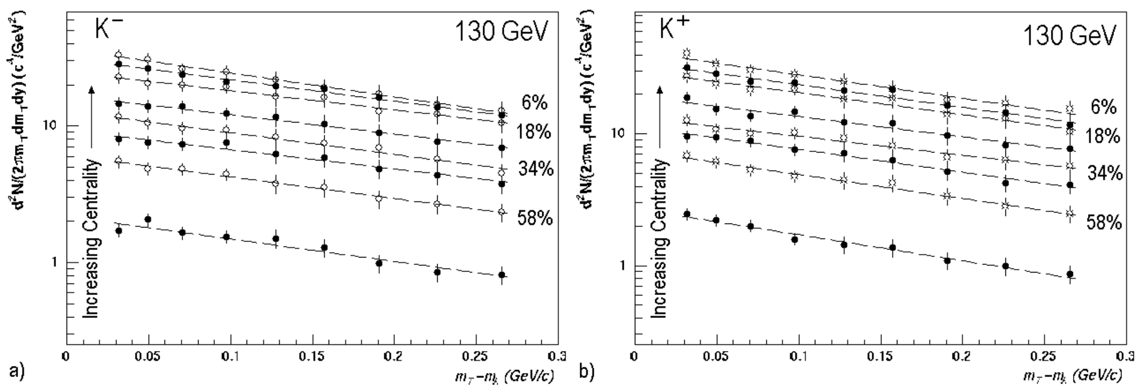

Figure 6.14 Corrected kaon yields from 130 GeV. Every other centrality bin is labeled starting with the top centrality. A 15% systematic error is included on points affected by electron contamination; a 10% systematic error is included for all other points.

Section 7

7.1 Kaon Ratio Results

After the kaon ratio has been calculated for each rapidity and pt bin, we can start looking for trends. We start by looking at how the ratio changes as a function of rapidity, p_t, and centrality. We will also look at the how the ratio changes with collision energy. The kaon ratio, along with several other particle ratios allows us to make a thermal model fit, and extract the chemical freeze-out temperature and baryo-chemical potential. We will also calculate the net-baryon number. A simple quark coalescence model will also be discussed as a tool to predict related ratios.

7.1.1 Ratio versus Rapidity

Figure 7.1 is a plot of all minimum bias data sets versus rapidity. Each rapidity bin is 0.1 units wide. The data are integrated over the entire transverse momentum range: 130 AGeV Au+Au - $100 < p_t < 600\,\mathrm{MeV/c}$, 200 AGeV Au+Au - $200 < p_t < 650\,\mathrm{MeV/c}$, and 200 GeV pp - $200 < p_t < 650\,\mathrm{MeV/c}$. The rapidity range covered, for all data, is $-0.4 < y < 0.4$. However in order to enhance statistics in the 130 AGeV Au+Au and 200 GeV pp data sets, the negative rapidity ($-0.4 < y < 0.0$) data has been added to the positive rapidity ($0.0 < y < 0.4$) data, resulting in an apparent rapidity range of $0.0 < y < 0.4$.

The ratios for each data set appear to be flat with respect to rapidity over this limited range. This result is consistent with the mid-rapidity $\bar{p}/p$ ratios observed in the same detector [Adl01c, Ada03d, Sch03].

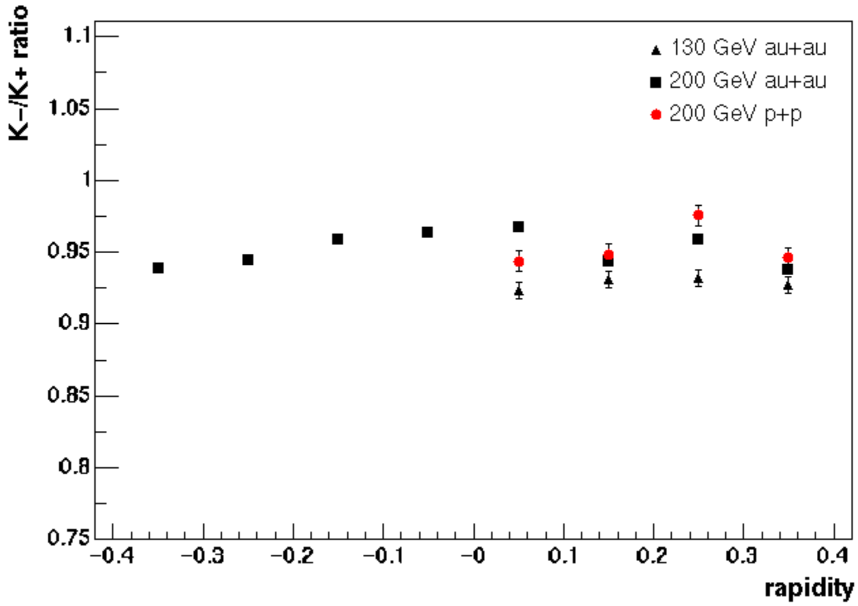

Figure 7.1 Kaon ratio versus rapidity. See text for description of the rapidity range covered for each data set. The ratios within each data set appear to be flat as a function of rapidity.

7.1.2 Ratio versus Transverse Momentum

Figure 7.2 is a plot of all minimum bias data sets versus transverse momentum. Each p_t bin is 50 MeV/c wide. The data is integrated over the entire rapidity range: $-0.4 < y < 0.4$. The transverse momentum range covered for each data set is: 130 AGeV Au+Au - $100 < p_t < 600\,\mathrm{MeV/c}$, 200 AGeV Au+Au - $200 < p_t < 650\,\mathrm{MeV/c}$, and 200 GeV pp - $200 < p_t < 650\,\mathrm{MeV/c}$.

The ratios appear to be flat with respect to transverse momentum. Again, this result is consistent with the mid-rapidity $\bar{p}/p$ ratios observed in the same detector [Adl01c, Sch03].

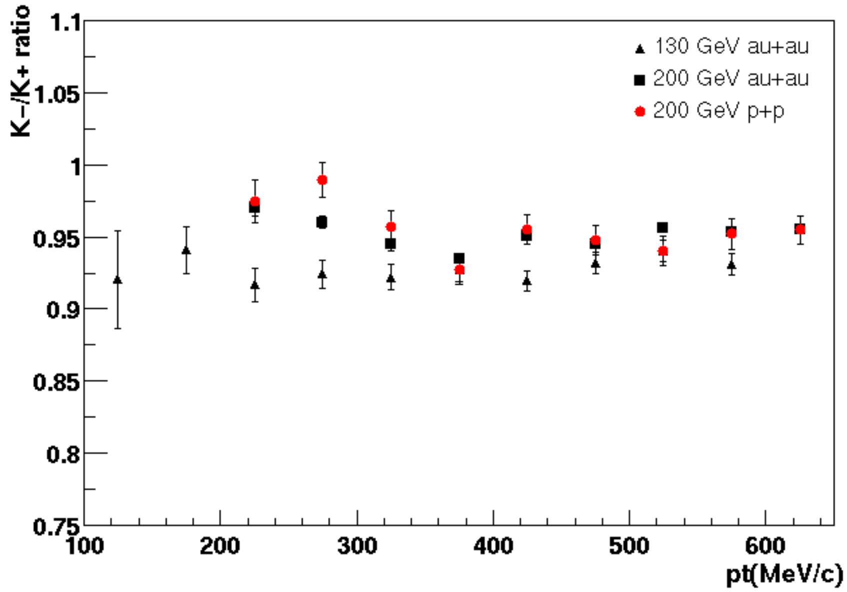

Figure 7.2 Kaon ratio versus transverse momentum. See text for description of the transverse momentum range covered for each data set. The ratios appear to be flat as a function of p_t.

7.1.3 Ratio versus Centrality

Figure 7.3 is a plot of the Au+Au data sets versus centrality. The data is integrated over the entire rapidity and p_t ranges (see above for details).

The *x*-axis is the number of negative hadrons, which is directly proportional to the collision centrality (see table 6.1). The 200 GeV pp data set is not divided into centrality bins since it has such a small range in multiplicity (see Fig. 6.3).

Both ratios show no significant dependence versus centrality. This result is also consistent with the mid-rapidity $\bar{p}/p$ ratios observed in the same detector [Adl01c, Sch03].

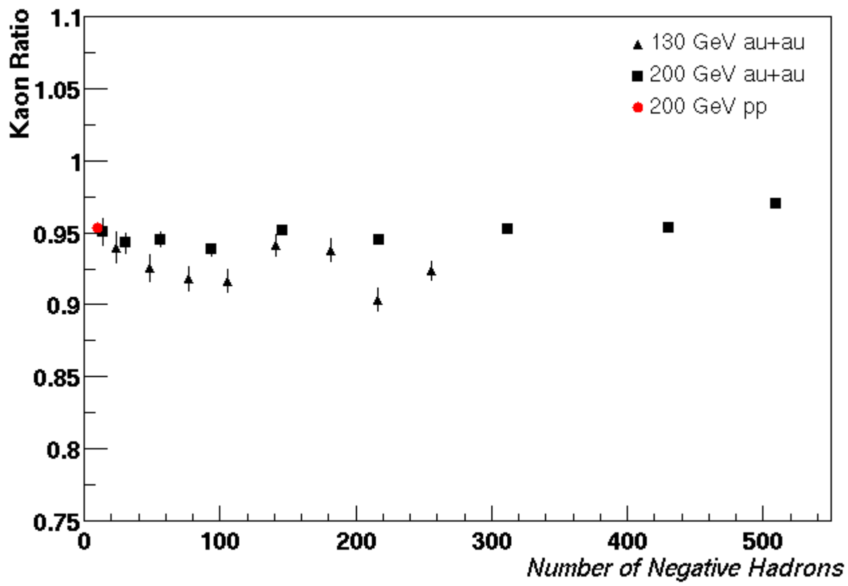

Figure 7.3 Kaon ratio versus number of negative hadrons. The ratios appear to be flat as a function of centrality.

7.1.4 Ratio versus Collision Energy

Figure 7.4 is a plot of the Au+Au data sets versus collision energy ($\sqrt{s_{NN}}$). The circles are from AGS experiments E866 and E917 [Ahl00]. The squares are from Pb+Pb collisions at the SPS from the NA49 experiment [Afa02]. The stars are the Au+Au STAR data reported here. Error bars shown include statistical and systematic errors; statistical errors are smaller than the marker size. The kaon ratio clearly increases as a function of $\sqrt{s_{NN}}$, asymptotically approaching unity at high energy. The STAR (RHIC) data have not yet reached the asymptotic value.

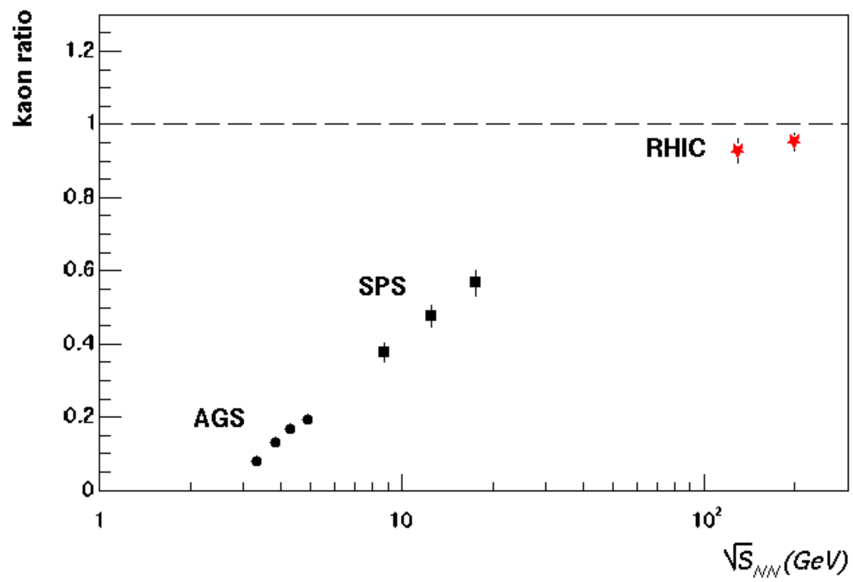

Figure 7.4 Kaon ratio vs. collision energy. Results from E866 and E917 are shown as circles, NA49 results are shown as squares, and STAR results are shown as stars.

Figure 7.5 shows the 200 GeV pp data versus collision energy ($\sqrt{s_{NN}}$), all data include statistical and systematic error bars. Lower energy results from the ISR [Ros75] show a trend continuing to RHIC energies. We can see that compared to RHIC energies, there are far fewer K^- with respect to K^+, hence a smaller K^-/K^+ ratio. As with the Au+Au collisions above, this can be attributed to the increased importance of the pair production over the associated production mechanism for the higher energy systems.

This shifting emphasis in production mechanisms creates a similarity between the Au+Au and pp data. In this respect, we can say that the heavy ion system is behaving like a scaled pp system. Each collision of Au+Au ions can be thought of as a large number of separate proton-proton collisions.

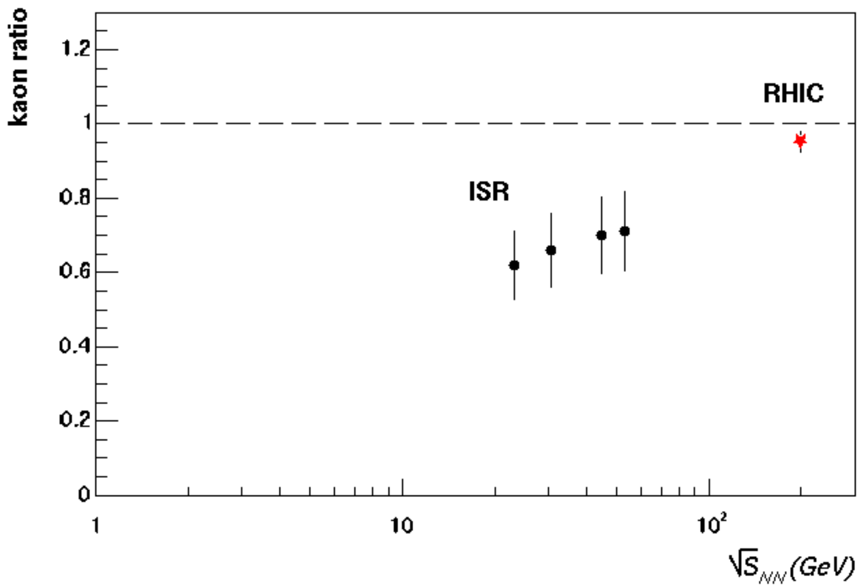

Figure 7.5 Kaon ratio vs. $\sqrt{s_{nn}}$ for pp collisions. Results from the CERN ISR [Ros75] are shown as circles and the STAR result is shown as a star.

7.1.5 Comparing Ratios at RHIC

All 4 experiments at RHIC have the ability to measure charged kaons, with differing acceptance and efficiency constraints. Figure 7.6 compares the results obtained by the different RHIC experiments. The dashed line for each collision system is the average of the published kaon ratios [Bac01, Vid02, Bea03, Baz01, Adl03a, Bac03]. The Au+Au data sets show good agreement between the experiments. The pp data set has only been reported by 2 experiments, STAR and PHENIX [Chu03]. The agreement is not as good as for Au+Au systems, however internal STAR analysis show much better agreement. The extent of agreement between the experiments suggests that no large "bugs" exist in our analysis.

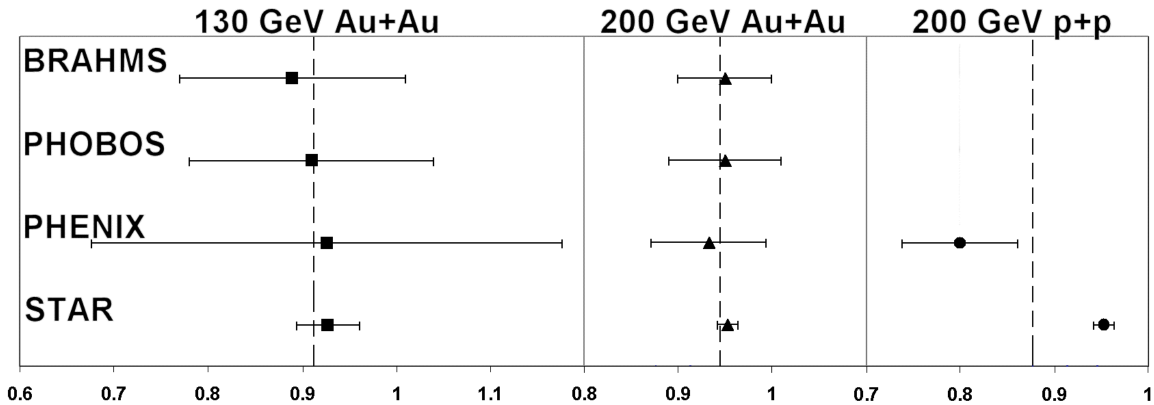

Figure 7.6 Comparison between the experiments at RHIC. The Au+Au data sets show good agreement. See text for references.

7.1.6 Discussion

The flat ratios have two main implications: (i) Both K^+ and K^- have similar transverse momentum distributions, meaning they "flow" together; (ii) The number of net-baryons is small, therefore the influence of the valence quarks is negligible. We can also state that since the K^-/K^+ ratio is very close to 1, particle pair production is the predominant mechanism for kaon production in high-energy collisions.

Collective flow was first observed in nuclear collisions at the Bevalac in Berkeley, CA [Gus84]. It is now a fairly well understood property of heavy ion collisions. There are two major forms of collective flow. The first is an isotropic radial flow, and the second is a non-isotropic streaming pattern of hadrons leading to the well-established "side splash" and "bounce-off" phenomena. The second type of flow (directed and elliptic) arises from the anisotropic expansion of the participant nucleons (Fig. 7.7), as well as the deflection of the collision spectators. The first type of flow (radial) is explained by a simple thermodynamic "fireball" model of the collision. In this view, the radial flow develops as a non-isentropic expansion resulting in transverse momentum spectra that, in the classical limit, are described by a Maxwell Boltzmann distribution determined by the source temperature.

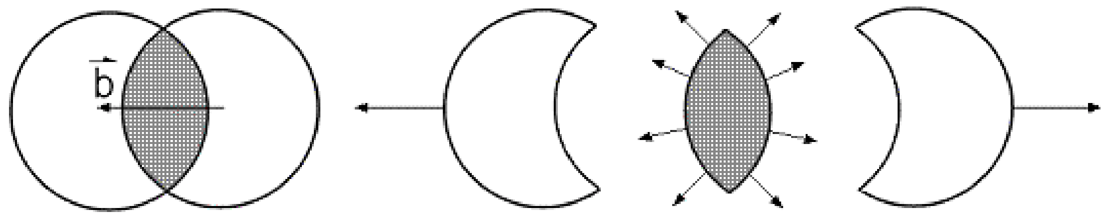

Figure 7.7 Schematic view of two colliding nuclei. The beam axis points into the drawing plane. The distance between the two ions is the impact parameter $\vec{b}$.

Particles can receive a “boost” in transverse momentum depending on their freeze-out dynamics. For example, if the K^- went through freeze-out earlier than the K^+ it would interact with an earlier, therefore high momentum, radial flow. We would expect to see such a situation manifest as an increase in high p_t K^- yields. This would lead to a non-flat kaon ratio versus p_t. However, since we observe a flat kaon ratio versus p_t, we can conclude that the K^+ and K^- freeze-out at approximately the same time.

Due to quark number conservation laws, we know that the number of quarks minus the number of anti-quarks must be constant. This means that any quarks created in the collision must be created as a quark - anti-quark pair. We can use this fact to obtain a qualitative estimate of the net-baryon density (density of quarks that came directly from the colliding ions). Since all K^+ from associated production must carry some of the original quark number, we know that the excess K^+ (when compared to the K^-) contributes to the net-baryon density [Bas03].

We can also make a statement about the competing kaon production mechanisms. The associated production mechanism, as discussed in section 2.4 can only produce K^+, while the pair production mechanism produces K^+ and K^-. So we can see that as the pair production mechanism begins to dominate, the K^- / K^+ ratio will begin to move toward 1. We can see from Fig. 7.4, the kaon ratio is smoothly approaching 1 as a function of the collision energy ($\sqrt{s_{NN}}$). We can clearly see that at RHIC, the pair production mechanism is dominant.

7.2 Thermal Model Fit

One of the questions we would like to answer is whether the strongly interacting nuclear, or possibly partonic, matter reaches the stage of chemical and thermal equilibrium. One of the possible approaches is to study the system with microscopic models. A more traditional way, which we will discuss further below, is to fit macroscopic experimental observables to the statistical model of a fully equilibrated hadron gas. If the hadron gas reaches chemical equilibrium, particle abundance is described by chemical potentials and temperature.

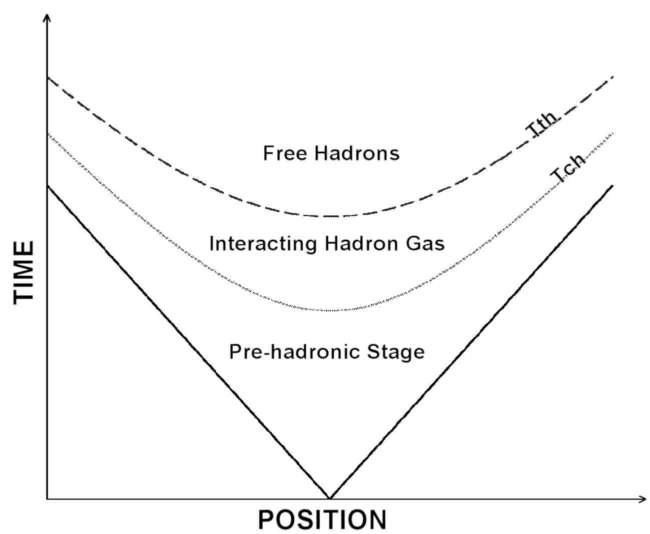

Figure 7.8 Stages of the space-time evolution of a heavy ion collision. At a certain moment in time (known as chemical freeze-out), hadrons emerge. The system then evolves as an interacting hadron gas, until thermal freeze-out, the point at which all elastic interactions cease as well.

7.2.1 Chemical Freeze-out Temperature and Baryo-Chemical Potential

Figure 7.8 is a schematic diagram of the evolution of a heavy ion collision. As the system evolves, hadrons emerge from the nuclear, or possibly partonic, matter. This is known as chemical freeze-out (T_{ch}). This is the point at which all inelastic collisions cease.

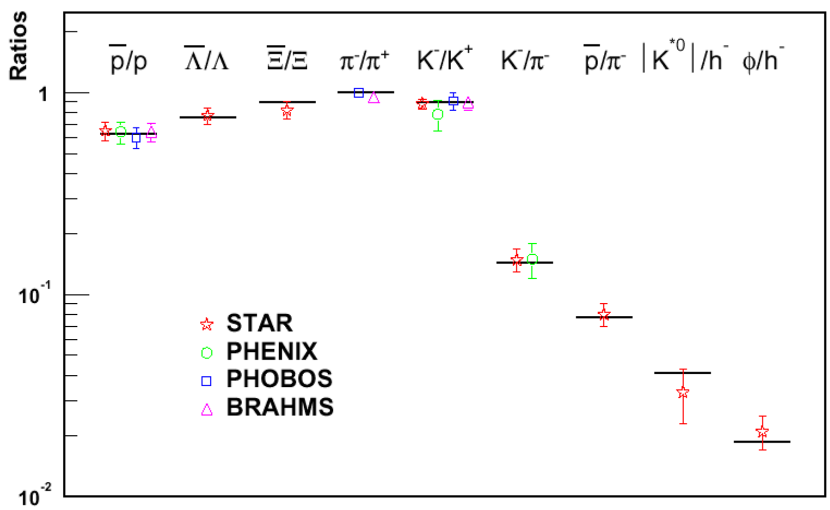

Figure 7.9 A thermal fit of several particle ratios for various ratios from the 130 GeV data set. The black line is the thermal prediction. Ratios are near mid-rapidity and not extrapolated to 4π [Xu02]

The chemical freeze-out temperature can be found by fitting various ratios to a statistical thermal model. Figure 7.9 shows the results of statistical model fit to several STAR ratios (fit performed by N. Xu, M. Kaneta [Xu02], and D. Magestro [Mag02]), the black line is the thermal model fit to the ratio. The model does a good job of fitting the data, suggesting that the hadron gas is near chemical equilibrium. The temperature and baryo-chemical potential extracted from the statistical fits are: $T_{ch} = 174 \pm 7\text{MeV}$, $\mu_B = 46 \pm 5\text{MeV}$ and $T_{ch} = 177 \pm 10\text{MeV}$, $\mu_B = 29 \pm 5\text{MeV}$ for 130 AGeV Au+Au and 200 AGeV Au+Au respectively.

The chemical freeze-out temperature changes very little from the SPS ($T_{ch} = 168 \pm 3\text{MeV}$ and $\mu_B = 266 \pm 5\text{MeV}$ [Bra99]), but the baryo-chemical potential decreases by a factor of 5-10; indicating far fewer net-baryons at RHIC energies. However, the agreement in temperature and lattice QCD predictions of the critical temperature T$_c$ ($T_c = 170 - 190\text{MeV}$ [Kar00]) suggests that both RHIC systems freeze-out directly to chemical equilibrium from the phase transition.

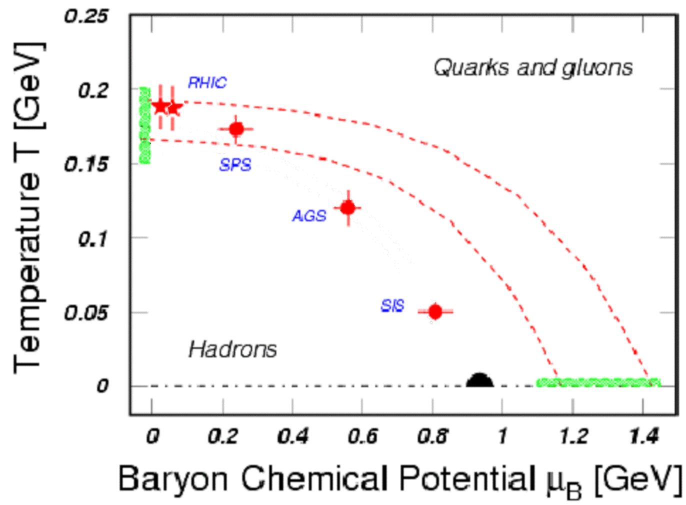

Figure 7.10 Chemical freeze-out temperature versus Baryo-chemical Potential. Lattice QCD predictions (dashed curves) suggest RHIC is nearing phase transition.

Figure 7.10 is a plot of the chemical freeze-out temperature versus the baryo-chemical potential for different collision systems. The 2 dashed lines represent the QCD prediction for the phase transition from a hadron phase to free quarks and gluons. The RHIC data points appear to continue a trend established from the lower energy experiments. The large black semi-circle at the bottom of the plot represents normal nuclear matter. The rectangle in the lower right represents conditions found inside neutron stars, while the upper left rectangle represents the conditions during the very early stages of the universe. This interpretation suggests that RHIC is very close to the phase transition. For a more a complete explanation of thermal models see [Xu02, Mag02, and Bra01].

7.3 Quark Coalescence Model

A significant increase in the number of quark degrees of freedom has been suggested as an indication of the quark-gluon plasma. If we assume that the probability of creating a baryon (or anti-baryon) is proportional to the probability that 3 quarks with appropriate quantum numbers meet at a certain location in phase-space, and if we also assume the quarks are uncorrelated (both assumptions are valid in thermal equilibrium), we obtain the following relationships [Bia98]:

$$p = \omega_P q^3 \,,\; \Lambda = \omega_\Lambda q^2 s \,,\; \Xi = \omega_\Xi q s^2 \,, \text{ and } \Omega = \omega_\Omega s^3$$

where:

q and s are the probabilities of finding a light quark and strange quark in the appropriate phase-space,

ω_i is a proportionality factor taking into account resonance and binding energies.

Similar formulas apply to anti-baryons. The ω_i factors are complex to calculate, and therefore direct comparisons with experimental data are difficult. However, if we consider only the ratio of the baryons to anti-baryons, the proportionality factors cancel. The result is:

$$\frac{\overline{p}}{p} = \frac{\overline{q}^3}{q^3} \,,\; \frac{\overline{\Lambda}}{\Lambda} = \frac{\overline{q}^2 \overline{s}}{q^2 s} \,,\; \frac{\overline{\Xi}^+}{\Xi^-} = \frac{\overline{q}\,\overline{s}^2}{q s^2} \,, \text{ and } \frac{\overline{\Omega}^+}{\Omega^-} = \frac{\overline{s}^3}{s^3} \,.$$

If we recognize that $K^+ = u\overline{s}$ and $K^- = \overline{u}s$, then with some rearrangement we can rewrite the above expressions as:

$$\frac{\overline{p}/p}{\overline{\Lambda}/\Lambda} = \frac{K^-}{K^+} \,,\; \frac{\overline{\Lambda}/\Lambda}{\Xi^-/\overline{\Xi}^+} = \frac{K^-}{K^+} \,, \text{ and } \frac{\Xi^-/\overline{\Xi}^+}{\Omega^-/\overline{\Omega}^+} = \frac{K^-}{K^+} \,.$$

The STAR 130 AGeV ratios are [Adl01c, Ada03a]:

$$\frac{\overline{p}}{p} = 0.65 \pm 0.08 \,,\; \frac{\overline{\Lambda}}{\Lambda} = 0.71 \pm 0.05 \,,\; \frac{\overline{\Xi}^+}{\Xi^-} = 0.83 \pm 0.09 \,, \text{ and } \frac{\overline{\Omega}^+}{\Omega^-} = 0.95 \pm 0.2 \,.$$

If we divide the ratios as illustrated above, we get:

$$\frac{\overline{p}/p}{\overline{\Lambda}/\Lambda} = 0.92 \pm 0.09, \ \frac{\overline{\Lambda}/\Lambda}{\Xi^-/\overline{\Xi}^+} = 0.86 \pm 0.11, \text{ and } \frac{\Omega^-/\overline{\Omega}^+}{\Xi^-/\overline{\Xi}^+} = 0.87 \pm 0.21.$$

These are in reasonable agreement with the 130 AGeV $K^-/K^+ = 0.928 \pm 0.03$. If we repeat the calculations using data from 158 GeV/c Pb+Pb collisions from the SPS [And99, Kan97, Afa02]:

$$\frac{\overline{p}}{p} = 0.07 \pm 0.01, \ \frac{\overline{\Lambda}}{\Lambda} = 0.133 \pm 0.007, \ \frac{\overline{\Xi}^+}{\Xi^-} = 0.249 \pm 0.019, \text{ and } \frac{\overline{\Omega}^+}{\Omega^-} = 0.383 \pm 0.081.$$

Dividing:

$$\frac{\overline{p}/p}{\overline{\Lambda}/\Lambda} = 0.53 \pm 0.3, \ \frac{\overline{\Lambda}/\Lambda}{\Xi^-/\overline{\Xi}^+} = 0.53 \pm 0.15, \text{ and } \frac{\Xi^-/\overline{\Xi}^+}{\Omega^-/\overline{\Omega}^+} = 0.65 \pm 0.15.$$

These show fair agreement with 158 GeV/c $K^-/K^+ = 0.57 \pm 0.06$. We can also compare these heavy ion systems to a mixed system p+Pb from the SPS [And99, Bea98]:

$$\frac{\overline{p}}{p} = 0.31 \pm 0.03, \ \frac{\overline{\Lambda}}{\Lambda} = 0.20 \pm 0.03, \text{ and } \frac{\overline{\Xi}^+}{\Xi^-} = 0.33 \pm 0.03$$

the Ω^-/Ω^+ ratio was not reported. Dividing:

$$\frac{\overline{p}/p}{\overline{\Lambda}/\Lambda} = 1.55 \pm 0.11, \text{ and } \frac{\overline{\Lambda}/\Lambda}{\Xi^-/\overline{\Xi}^+} = 0.61 \pm 0.07.$$

Unfortunately I could not find a reported K^-/K^+, but it is clear that the agreement would be much worse than the heavy ion data reported above. This can be interpreted as an indication that the quark degrees of freedom do not represent a large factor in the production mechanisms, for the p+Pb system.

7.4 Kaon Yields

As discussed in section 2.3.2 strangeness enhancement is a possible signature of the QGP. This section reports the integrated yields (dN/dy) and the inverse slope parameter (T) as a function of the number of negative hadrons ($dN_{h^-}/d\eta$), extracted from the corrected kaon yields reported in section 6.10. The yields and inverse slope parameters will be compared with results from the AGS and SPS. The kinetic (thermal) freeze-out temperature will be extracted from the inverse slope parameter.

7.4.1 Integrated Yield and Inverse Slope Parameter

Figure 7.11 is a plot of $\frac{dN/dy}{dN_{h^-}/d\eta}$ versus number of negative hadrons ($dN_{h^-}/d\eta$). The shape of $\frac{dN/dy}{dN_{h^-}/d\eta}$ for K^+ and K^- exhibit the same shape within each collisions system, suggesting that they have similar production mechanisms and flow dynamics. We can also see that this ratio increases slightly as a function of centrality. This slight increase may be due to the difference in longitudinal expansion between the peripheral and central collisions. However, at lower energies (AGS and SPS [Ahl99, Ahl98]) this ratio nearly doubles from peripheral to central collisions. Since, the longitudinal expansion is expected to be larger at RHIC, due to the increased energy density expected, perhaps the larger increase at lower energies indicates a change in the kaon production mechanism over centrality. On the other hand, the kaon ratio (K^-/K^+) remains constant as a function of centrality, at all energies suggesting a consistent production mechanism. The increase may be attributed to the larger importance of hadronic scattering in the lower energy collisions. Leading to a kaon production enhancement in more central collisions.

The pp data point is much lower than the Au+Au data, reflecting the lower kaon yield in pp collisions.

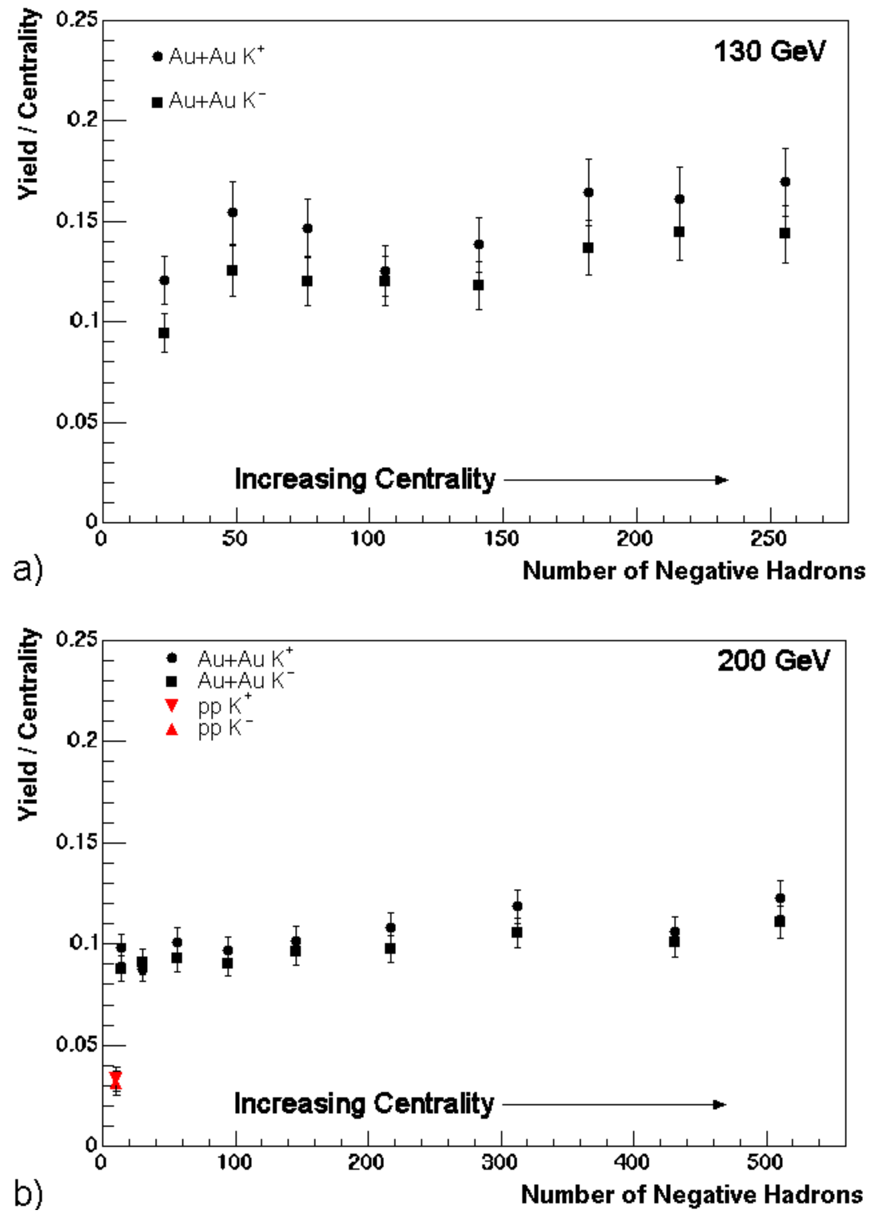

Figure 7.11 The ratio of dN/dy to $dN_{h^-}/d\eta$ for (a) 130 AGeV Au+Au and (b) 200 AGeV Au+Au and pp data. Both ratios appear to increase slightly as a function of centrality. Error bars include statistical and systematic errors.

Figure 7.12 is a plot of the inverse slope parameter versus centrality. The slope parameter appears to be flat for the 130 AGeV data (a slight bump can be seen, but is most likely not a physical feature) and shows an increase from around 200 MeV to 300 MeV for the 200 AGeV data.

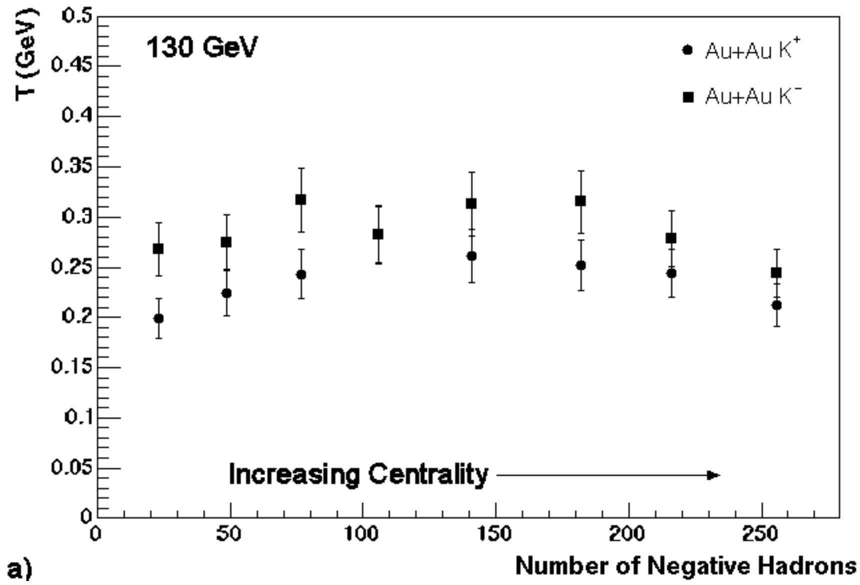

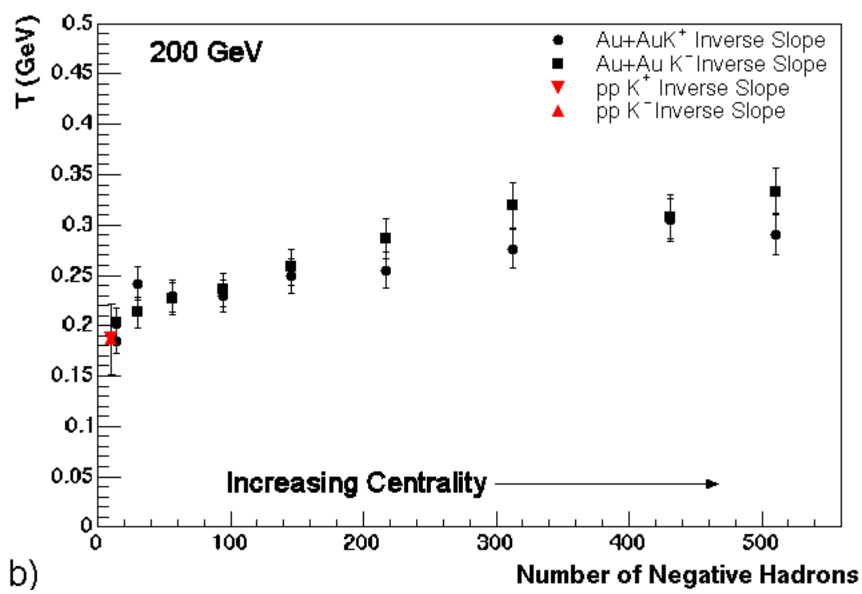

Figure 7.12 The inverse slope parameter versus the number of negative hadrons. The (a) 130 AGeV data is consistent with a flat line, while the (b) 200 AGeV data increases from peripheral to central collisions. The pp data is also shown in (b). Error bars include statistical and systematic errors.

The pp data agree well with the most peripheral Au+Au data. Supporting the suggestion from section 7.1.4, that the Au+Au data may act as many single pp collisions.

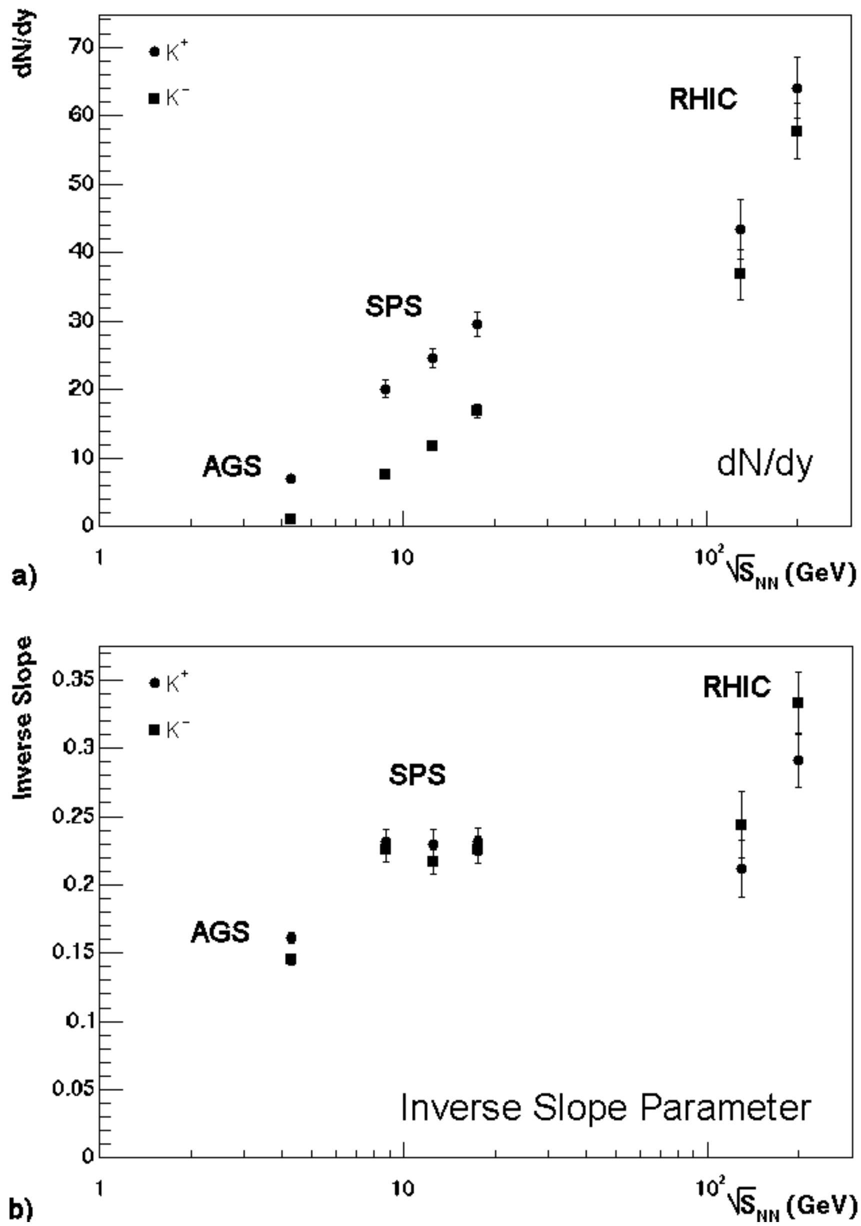

Figure 7.13 (a) is a plot of the rapidity density at mid-rapidity for several different collision energies. (b) is a plot of the inverse slope parameter versus collision energy. All data shown is from the top centrality bin. Error bars include statistical and systematic errors.

Table 7.1 lists dN/dy and T versus number of negative hadrons. The table includes a 15% systematic error for the 130 AGeV Au+Au data, a 7% systematic error for the 200 AGeV Au+Au data, and a 20% systematic error for the 200 GeV pp data; the systematic errors were estimated using the m_t fit to the data. We can compare this data to lower energy collisions from the AGS and SPS [Ahl98, Afa02], included in table 7.1.

Figure 7.13a is a plot of the dN/dy versus collision energy for the top centrality bin. We can see an increase in the yield as the collision energy increases. Figure 7.13b is a plot of the inverse slope parameter versus collision energy. Again, the data appears to increase from AGS energy and peak at the top RHIC energy. In both plots, the 130 AGeV data appears to lie slightly below the apparent trend.

The inverse slope parameter is a combination of the kinetic freeze-out temperature and the radial flow velocity. A simple relationship exists to relate the inverse slope temperature to the thermal freeze-out temperature:

$$T = T_{fo} + C \cdot m\langle \beta \rangle^2$$

where:

T is the inverse slope parameter,

T_{fo} is the thermal freeze-out temperature,

C is a constant,

m is the particle rest mass, and

$\langle\beta\rangle$ is the average collective flow velocity.

Using the above relation, with $C = 0.7$, the thermal freeze-out was calculated for the 200 GeV Au+Au data. Using average collective flow velocities provided by K. Schweda: from peripheral to central collisions {0.36±0.02, 0.42±0.02, 0.47±0.01, 0.50±0.01, 0.53±0.01, 0.56±0.01, 0.57±0.00, 0.58±0.01, and 0.59±0.01}. The above relationship is only expected to provide a qualitative result at RHIC, due to large re-scattering. Figure 7.15 is the result of a hydrodynamic analysis performed on the 200 GeV Au+Au data by N. Xu [Xu03]. The trend of decreasing thermal freeze-out temperature agrees with the qualitative trend shown in Fig. 7.14.

A thermal analysis that included pion, kaon, and proton transverse spectra determined the kinetic freeze-out temperature to be $T_{fo} = 100 \pm 20 MeV$ for 130 AGeV [Xu02]. A more sophisticated analysis taking a hydrodynamic approach, also including the pion, kaon, and proton spectra, found $T_{fo} = 89 \pm 10 MeV$ for 200 AGeV [Ada03b].

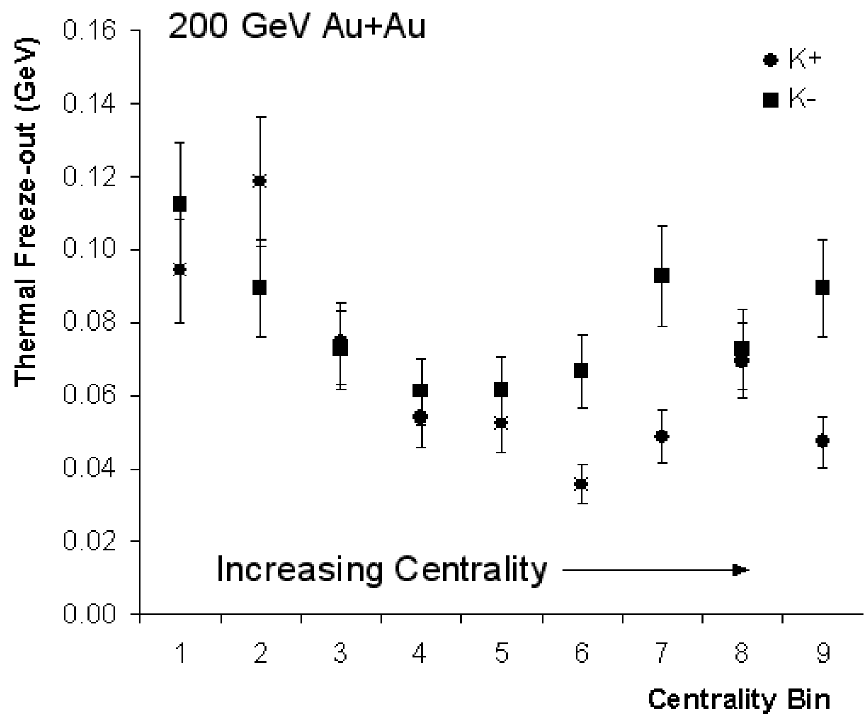

Figure 7.14 Thermal freeze-out temperature vs. centrality. Calculated using empirical relationship above. A decrease can be seen as a function of centrality, from ~0.110 GeV to ~0.080 GeV.

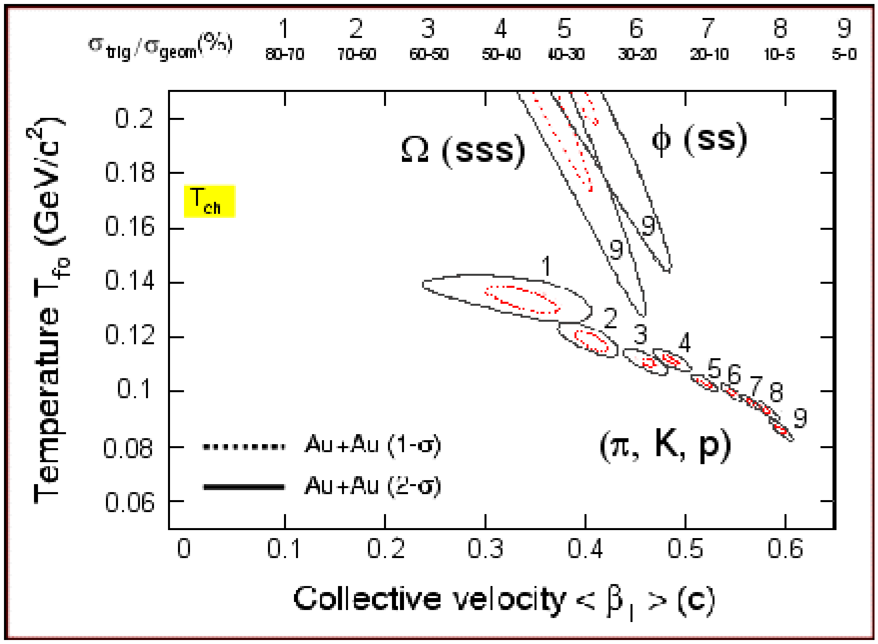

Figure 7.15 Thermal freeze-out temperature versus collective flow velocity. The data presented here is from an hydrodynamic analysis performed by N. Xu [Xu03].

Figure 7.16a shows the trend of kinetic freeze-out temperature versus energy. The temperature rises quickly to around 150 MeV, at the SPS then seems to decrease at RHIC energies. We see a similar trend in Fig. 7.16b with the average collective flow versus the collision energy, a steep rise, plateau at SPS, but a strong increase to RHIC energies.

The large difference between the chemical freeze-out (~175 MeV) and thermal freeze-out (~100 MeV) temperatures and the development of a strong collective flow component suggest a significant expansion and significant duration from chemical to kinetic freeze-out in central collisions. This creates a picture of RHIC collisions with varying initial conditions evolving toward the same chemical freeze-out temperature followed by further cooling and expansion.

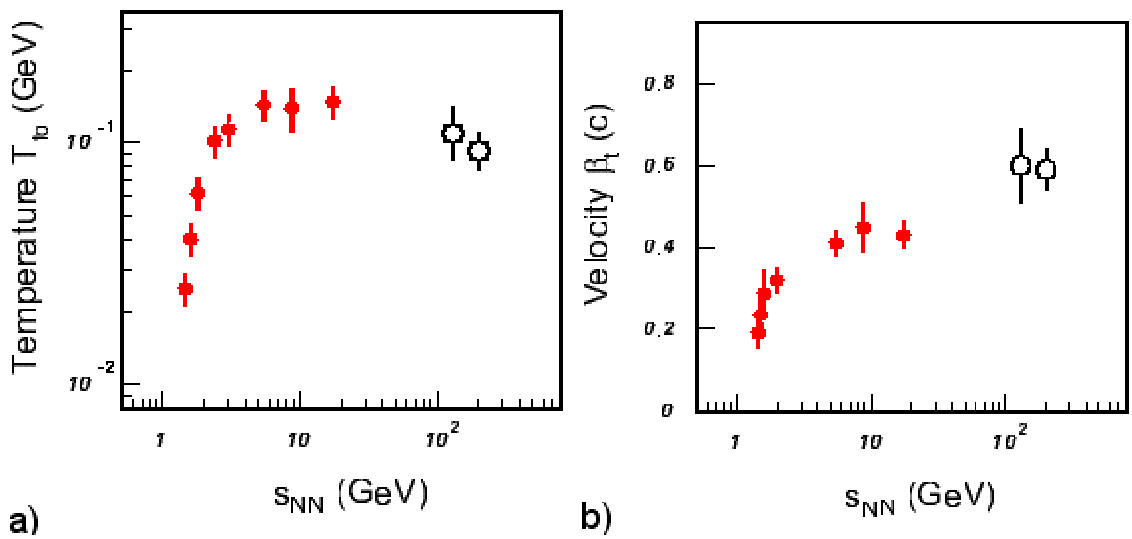

Figure 7.16 (a) The thermal freeze-out temperature versus energy. A sharp increase evolves to a plateau at SPS energies followed by a decrease at RHIC energies. (b) Average collective flow velocity versus energy. We see a plateau at SPS energies and an increase at RHIC [Xu02].

Table 7.1 Rapidity densities (dN/dy) and inverse slope parameter (T) at mid-rapidity from the data presented here as well as from the most central collisions at the AGS and SPS [Ahl98, Afa02].

	K^+		K^-	
	130 AGeV Au+Au			
# Neg. Hadrons	dN/dy	T (GeV)	dN/dy	T (GeV)
23	2.80±0.28	0.199±0.020	2.19±0.22	0.268±0.027
48	7.50±0.75	0.224±0.022	6.09±0.61	0.275±0.028
76	11.20±1.12	0.243±0.024	9.20±0.92	0.317±0.032
106	13.30±1.33	0.282±0.028	12.75±1.28	0.283±0.028
141	19.50±1.95	0.261±0.026	16.65±1.67	0.313±0.031
182	29.90±2.99	0.252±0.025	24.88±2.49	0.315±0.032
216	34.80±3.48	0.244±0.024	31.29±3.13	0.278±0.028
256	43.40±4.34	0.212±0.021	36.78±3.68	0.244±0.024

		200 AGeV Au+Au		
14	1.37±0.10	0.185±0.013	1.76±0.12	0.203±0.014
30	2.63±0.18	0.242±0.017	3.36±0.24	0.213±0.015
56	5.66±0.40	0.229±0.016	5.70±0.40	0.227±0.016
94	9.08±0.64	0.229±0.016	8.88±0.62	0.236±0.017
146	14.80±1.04	0.249±0.017	12.51±0.88	0.258±0.018
217	23.45±1.64	0.255±0.018	19.08±1.34	0.286±0.020
312	36.98±2.59	0.276±0.019	28.76±2.01	0.320±0.022
431	45.72±3.20	0.305±0.021	44.43±3.11	0.308±0.022
519	62.50±4.37	0.291±0.020	57.73±4.04	0.333±0.023
		200 GeV pp		
10	0.33±0.06	0.187±0.037	0.31±0.06	0.187±0.037
		AGS 11.6 GeV/c		
Most Central	6.89±0.29	0.161±0.004	1.12±0.05	0.145±0.004
		SPS 40, 80, 158 GeV		
Most Central	20.1±1.3	0.232±0.009	7.58±0.52	0.226±0.009
	24.6±1.4	0.230±0.011	11.7±0.70	0.217±0.009
	29.6±1.8	0.232±0.010	16.8±1.00	0.226±0.010

Section 8

8.1 Conclusions

We have studied the charged kaon ratio, spectra, rapidity densities, and inverse slope parameter at mid-rapidity in Au+Au collisions at $\sqrt{s_{NN}} = 130\mathrm{GeV}$ and $\sqrt{s_{NN}} = 200\mathrm{GeV}$ and pp collisions at $\sqrt{s_{NN}} = 200\mathrm{GeV}$.

The kaon ratio is close to 1 and shows no dependence on rapidity, transverse momentum, and centrality over the ranges studied. The trend from lower energy experiments at the AGS and SPS seems to continue at RHIC as we asymptotically approach unity.

The ratio for the Au+Au data sets is in good agreement with results from the other experiments at RHIC (BRAHMS, PHOBOS, and PHENIX). The ratio for the pp data set is higher than the reported ratio for PHENIX (the only other pp result available), however the large error bars indicate some uncertainty in their result. Internal analysis within the STAR experiment shows much better agreement.

The flat ratios indicate that the production mechanism does not change across centrality. It also suggests that the K^{+} and K^{-} undergo similar collective flow. This result agrees with what we see at lower energies, where the kaon ratio is also flat as a function of centrality. However, re-scattering is much more important at lower energies and may be responsible for the flat kaon ratio versus centrality.

We can also conclude that since the ratio is nearly 1, the collision is almost net-baryon free at mid-rapidity. The measured kaon ratio shows agreement with other strange ratios measured in the same detector using a simple quark coalescence model. Using the $p/\overline{p}$ ratio to set the baryo-chemical properties, the K^{+}/K^{-} ratio can predict the other strange ratios. The success of this model indicates the importance of the quark degrees of freedom at higher energy collisions during particle production.

A thermal model fit does a good job describing the data and allows us to extract two important parameters, chemical freeze-out temperature (T_{ch}) and baryo-chemical potential (μ_{B}). The chemical freeze-out temperature was found to be ≈175 MeV and shows little increase over lower energies. The baryo-chemical potential showed a large decrease from SPS to RHIC, indicating a considerable decrease in the number of net-baryons at mid-rapidity. A plot of T_{ch} versus μ_{B} shows RHIC continuing a trend established from lower energy experiments. If we are allowed to make the assumption that equilibrium is reached shortly after the collision occurs we can use these parameters to indicate that we are approaching the QCD predicted phase transition.

The kaon yields were well described by an exponential in m_t, over our limited range. The shape was consistent between K^{+} to K^{-}, and changed very little between centrality bins. This reinforces the suggestion from above that the production mechanism for the kaon is not changing from peripheral to central collisions.

The rapidity density (dN/dy) was extracted from the m_t fits. The result was divided by the number of negative hadrons and plotted versus the number of negative hadrons. This plot showed a slight increase versus centrality. This increase is most likely due to the difference in longitudinal expansion between peripheral and central collisions. The pp analysis produced a $\frac{dN/dy}{dN_{h^-}/d\eta}$ ratio that was much lower than the peripheral Au+Au result. This is expected since, much less energy is available in the pp collision to produce the strange quark.

The inverse slope parameter (*T*) was also extracted from the m_t fits and plotted versus centrality. We saw a small increase in *T* versus centrality for the 200 AGeV Au+Au data, but the 130 AGeV Au+Au data remained flat (with a small unexplained hump). The pp data showed a remarkable agreement with the peripheral Au+Au data. This provides support for picturing Au+Au collisions as multiple separate pp collisions (especially at large impact parameters).

Plots comparing the dN/dy and the inverse slope parameter with lower energy experiments showed an increasing trend from lower energy to RHIC energies. This trend reflects the increased yield expected in the higher density collisions at RHIC as well as the increased collective flow in these collisions. The trends seen in Fig. 7.13 suggest the 130 AGeV Au+Au data results are slightly low. This deviation from the trend (if it is real) is unexplained.

The slope parameter is a primarily a combination of the thermal freeze-out temperature (T_{fo}) and the radial flow velocity, and can be related using a simple qualitative relationship. Using this relationship and average collective flow velocities, the thermal freeze-out was plotted versus centrality for the 200 GeV Au+Au data. The trend shown in this plot agreed with the trend seen for a much more sophisticated analysis performed by N. Xu. Results from full analyses, that included fits to pions, kaons and protons, found the T_{fo} to be ~100 MeV for 130 AGeV Au+Au and ~89 MeV for 200 AGeV Au+Au. A comparison with lower energy experiments showed a rapid increase rising to a plateau at SPS energies, with a slight decrease at RHIC's top energy.

A similar plot for the collective flow velocity showed the same trend, a strong increase followed by a plateau at SPS energies, however, the collective flow increases at RHIC. This increase is an indication of a stronger, more violent expansion.

Bibliography

[Ack01] K.H Ackermann *et al.*, "Elliptic Flow in Au+Au Collisions at $\sqrt{s_{NN}} = 130\text{GeV}$ ", Phys. Rev. Lett. **86**, 402 (2001).

[Ack03a] K.H. Ackermann *et al.*, "STAR Detector Overview", Nucl. Instrum. Meth. A **499**, 624 (2003).

[Ack03b] K.H. Ackermann et al., "The Forward Time Projection Chambers in STAR", Nucl. Instrum. Meth. A **499**, 713 (2003).

[Ada03a] J. Adams *et al.*, "Strange Antiparticle-to-Particle ratios at Mid-Rapidity in $\sqrt{s_{NN}} = 130\text{GeV}$ Au+Au Collisions", Phys. Lett. B **567**, 167 (2003).

[Ada03b] J. Adams *et al.*, "Identified Particle Distribution in pp and Au+Au Collisions at $\sqrt{s_{NN}} = 200\text{GeV}$", in STAR publication committee (2003).

[Ada03c] J. Adams *et al.*, "Multiplicity Fluctuations in Au+Au Collisions at sqrt(snn)=130 GeV", submitted to Phys. Rev. C 07/06/03 [nucl-ex/0307007].

[Ada03d] J. Adams *et al.*, "Erratum: Midrapidity Antiproton-to-Proton Ratio from Au+Au sqrt(s_{nn}) = 130 GeV", Phys. Rev. Lett. **90**, 119903 (2003). Corrects [Adl01c].

[Adc01] K. Adcox *et al.*, "Measurement of the Midrapidity Transverse Energy Distribution from $\sqrt{s_{NN}} = 130\text{GeV}$ Au+Au Collisions at RHIC", Phys. Rev. Lett. **87**, 052301 (2001).

[Adl01a] C. Adler *et al.*, "The RHIC Zero Degree Calorimeters", Nucl. Instrum. Meth. A **470**, 488 (2001).

[Adl01b] C. Adler *et al.*, "Multiplicty Distribution and Spectra of Negatively Charged Hadrons in Au+Au Collisions at $\sqrt{s_{NN}} = 130\text{GeV}$ ", Phys. Rev. Lett. **87**, 112303 (2001).

[Adl01c] C. Adler *et al.,* "Midrapidity Antiproton-to-Proton Ratio from Au+Au qsrt(s_{NN})=130GeV", Phys. Rev. Lett. **86**, 4778 (2001). See [Ada03d] for correction.

[Adl03a] S.S. Adler *et al.*, "Identified Charged Particle Spectra and Yields in Au+Au Collisions at $\sqrt{s_{NN}} = 200\text{GeV}$", nucl-ex/0307022, (2003).

[Adl03b] C. Adler *et al.*, "Disappearance of Back-to-Back High p_T Hadron Correlations in Central Au+Au Collisions at sqrt(snn) = 200 GeV", Phys. Rev. Lett. **90**, 082302 (2003).

[Afa02] S.V. Afanasiev *et al.*, "Energy Dependence of Pion and Kaon Production in Central Pb+Pb Collisions", Phys. Rev. C **66**, 054902 (2002).

[Ahl00] L. Ahle *et al.,* "An Excitation Function of K^- and K^+ Production in Au+Au Reactions at the AGS", Phys. Lett. B **490**, 53 (2000).

[Ahl98] L. Ahle *et al.*, "Kaon Production in Au+Au Collisions at 11.6A GeV/c", Phys. Rev. C **58**, 3523 (1998).

[Ahl99] L. Ahle *et al.*, "Centrality Dependence of Kaon Yields in Si+A and Au+Au Collisions at Relativistic Energies", Phys. Rev. C **60**, 044904 (1999)

[Alb95] T. Alber *et al.*, "Transverse Energy Production in ^{208}Pb+Pb Collisions at 158 GeV per Nucleon", Phys. Rev. Lett. **75**, 3814 (1995).

[And03] M. Anderson *et al.*,"The STAR Time Projection Chamber", Nucl. Instrum. Meth. A **499**, 659 (2003).

[And99] E. Andersen *et al.*, "Λ, Ξ, and Ω Production at Mid-Rapidity in Pb-Pb and p-Pb collisions at 158 A GeV/c", J. Phys. G **25**, 171 (1999).

[Atw91] W.B. Atwood *et al.*, "Tracking with the ALEPH Time Projection Chamber", IEEE Trans. Nucl. Sci. **38**, 432 (1991).

[Bac01] B.B. Back *et al.*, "Ratios of Charged Antiparticles-to-Particles near Mid-Rapidity in Au+Au Collisions at $\sqrt{s_{NN}} = 130\text{GeV}$ ", Phys. Rev. Lett. **87**, 102301 (2001).

[Bac03] B.B. Back *et al,*. "Ratios of Charged Antiparticles to Particles near Midrapidity in Au+Au Collisions at $\sqrt{s_{NN}} = 200\text{GeV}$", Phys. Rev. C **67**, 021901, (2003).

[Bar03] O. Barannikova, Purdue University and the STAR collaboration, private communication, 2003.

[Bas03] S.A. Bass *et al.*, "Net Baryon in Au+Au Collisions at the Relativistic Heavy Ion Collider", Phys. Rev. Lett. **91**, 052302 (2003).

[Baz01] A. Bazilevsky, "First Results from PHENIX at RHIC", Proceedings of XXXVI Rencontres de Moriond: QCD, (2001).

[Bea03] I.G. Bearden *et al,*. "Rapidity Dependence of Charged Antihadron to Hadron Ratios in Au+Au Collisions at $\sqrt{s_{NN}} = 200\text{GeV}$", Phys. Rev. Lett. **90**, 102301 (2003).

[Bea98] I.G. Bearden *et al.*, "Proton and Antiproton Distributions at Midrapidity in Proton-Nucleus and Sulphur-Nucleus Collisions", Phys. Rev. C **57**, 837 (1998).

[Bel03] R. Bellwied *et al.*, "The STAR Silicon Vertex Tracker", Nucl. Instrum. Meth. A **499**, 640 (2003).

[Bev92] P.R. Bevington and D.K. Robinson, Data Reduction and Error Analysis for the Physical Sciences Boston: McGraw-Hill, 1992.

[Bia98] A. Bialas, "Quark Model and Strange Baryon Production in Heavy Ion Collisions", Phys. Lett. B **442**, 449 (1998).

[Bie03] F.S. Bieser *et al.*, "The STAR Trigger", Nucl. Instrum. Meth. A **499**, 766 (2003).

[Boc90] R.K. Bocke *et al.*, Data Analysis Techniques for High-Energy Experiments Cambridge: Cambridge University Press, 1990.

[Bra01] P. Braun-Munzinger *et al.*, "Hadron Production in Au-Au Collisions at RHIC", Phys. Lett. B **518**, 41 (2001).

[Bra03] A. Braem et al.,"Identification of High Pt Particles with the STAR-RICH Detector", Nucl. Instrum. Meth. A **499**, 720 (2003).

[Bra99] P. Braun-Munzinger *et al.*, "Chemical Equilibration in Pb+Pb Collisions at the SPS", Phys. Lett B **465**, 15 (1999).

[Bre69] M. Breidenbach *et al.*, " Observed Behavior of Highly Inelastic Electron-Proton Scattering", Phys. Rev. Lett. **23**, 935 (1969).

[Cal01] M. Calderón de la Barca Sánchez, *Charged Hadron Spectra in Au+Au Collisions at* $\sqrt{s_{NN}} = 130\text{GeV}$. Ph. D. Thesis, Yale University, 2001 (unpublished).

[Car02] A. Cardenas, *Charged Kaon Production at Mid-Rapidity in Gold-Gold Collisions at 130 GeV.* Ph. D. Thesis, Purdue University, 2002 (unpublished).

[Ceb92] D. Cebra and S. Margetis, Technical Report, STAR Note 89, Main Vertex Reconstruction in STAR (unpublished), 1992).

[Chu03] T. Chujo, "Results on Identified Hadrons from the PHENIX Experiment at RHIC", Nuclear Physics A **715**, 151c-160c (2003).

[Gar89] C. Garabatos *et al.*, "A TPC in the Context of Heavy-Ion Collisions", Nucl. Instrum. Methods Phys. Res. A **283**, 553 (1989).

[Gel64] M. Gell-Mann, "A Schematic Model of Baryons and Mesons", Phys. Lett. **8**, 214 (1964).

[Gus84] H.A. Gustafsson *et al.*, "Collective Flow Observed in Relativistic Nuclear Collisions", Phy. Rev. Lett. **52**, 1590 (1984).

[Gyu94] M. Gyulassy and X. Wang, "Multiple Collisions and Induced Gluon Bremsstrhlung in QCD", Nucl. Phys. B **420**, 583 (1994).

[Hag02] K. Hagiwara *et al.*, “The Review of Paricle Physics 2002 Edition”, Phys. Rev. D **66**, 010001-1 (2002).

[Har96] J.W. Harris and B. Müller, “The Search for the Quark-Gluon Plasma”, Annu. Rev. Nucl. Sci. **46**, 71 (1996).

[Kan97] M. Kaneta *et al.*, “Particle Ratios from Central Pb-Pb Collisions at the CERN SPS”, J. Phys. G **23**, 1865 (1997).

[Kar00] F. Karsch, “Lattice QCD at Finite Temperature and Density”, Nucl. Phys. B **83**, 14 (2000).

[Kir02] J. Kiryluk *et al.*, “Relative Luminosity Measurement in STAR and Implications for Spin Asymmetry Determinations” In SPIN2002: 15th International Spin Physics Symposium, 2002.

[Kno89] G. Knoll, <u>Radiation Detection and Measurement</u> New York: John Wiley & Sons, 1989.

[Kol90] E. Kolb and M.S. Turner <u>The Early Universe.</u> Redwood City, CA: Addison-Wesley, 1990.

[Kot03] L. Kotchenda *et al.*, “STAR TPC Gas System”, Nucl. Instrum. Meth. A **499**, 703 (2003).

[Lan03] J.M. Landgraf *et al.*, “An Overview of the STAR DAQ System”, Nucl. Instrum. Meth. A **499**, 762 (2003).

[Las97] B. Lasiuk, Technical Report, STAR Note 312, Particle Identification at STAR (unpublished),1997.

[Leb03] A. Lebedev *et al.*, “The STAR Laser System”, Nucl. Instrum. Meth. A **499**, 692 (2003).

[Lis96] M.A. Lisa, Technical Report, STAR Note 238, The STAR-TPC Clusterfinder / Hitfinder (unpublished), 1996.

[Mag02] D. Magestro, “Evidence for Chemical Equilibration at RHIC”, J. Phys. G **28**, 1745 (2002).

[Mat03] H.S. Matis *et al.*, “Integration and Conventional Systems at STAR”, Nucl. Instrum. Meth. A **499**, 802 (2003).

[Mat86] T. Matsui and H. Satz, “J/psi Suppression by Quark-Gluon Plasma Formation”, Phys. Lett. B **178**, 416 (1986).

[Mat90] J.C. Mather *et al.*, “A Preliminary Measurement of the Cosmic Microwave Background Spectrum by the Cosmic Background Explorer (COBE) Satellite”, Astrophys. J. Lett. **354**, L37 (1990).

[Oza91] S. Ozaki, "RHIC Project", *Conference Record of the 1991 IEEE Particles Accelerator Conference.* New York, NY, USA: IEEE 5 vol. **3283**, 2901-4 (1991).

[Raf82] J. Rafelski and B. Müller, "Strangeness Prodution in the Quark-Gluon Plasma", Phys. Rev. Lett. **48**, 1066 (1982).

[Rol93] L. Rolandi and W. Blum. Particle Detection with Drift Chambers Berlin: Springer-Verlag, 1993.

[Ros02] T. Roser, "RHIC Performance", Nuclear Physics A **698**, 23c-28c (2002).

[Ros75] A.M. Rossi and G. Vannini, "Experimental Study of the Energy Dependence in Proton-Proton Inclusive Reactions", Nucl. Phys. B **84,** 269 (1975).

[Rut11] E. Rutherford, "The Scattering of α and β Particles by Matter and the Structure of the Atom", Phil. Mag. **21**, 669 (1911).

[Sak94] I.M. Sakrejda and J.T. Mitchell, Technical Report, STAR Note 190, Tracking for the STAR TPC: Documentation and User's Guide (unpublished), 1994.

[Sch03] K. Schweda, Lawrence Berkeley Laboratory and the STAR collaboration, private communication, 2003.

[Ste01] F.D. Steffen and M.H. Thoma, " Hard Thermal Photon Production in Relativistic heavy Ion Collisions", Phys. Lett. B **510**, 98 (2001).

[Van98] S.E. Vance *et al.*, "Baryon Number Transport via Gluonic Junctions", Phys. Lett. B **443**, 45 (1998).

[Vid02] F. Videbæk *et al.*, "Results from the BRAHMS experiment at RHIC", Nuclear Physics A **698**, 29c-28c (2002).

[Wil97] W.K. Wilson *et al.*, Technical Report, STAR Note 299, The Impact of the SVT Material on the TPC Environment (unpublished).

[Won94] C. Wong, Introduction to High-Energy Heavy-Ion Collisions Singapore: World Scientific, 1994.

[Xu02] N. Xu and M. Kaneta, "Hadron Freeze-out Conditions in High Energy Nuclear Collisions", Nucl. Phys. A **698**, 306c (2002).

[Xu03] N. Xu, Lawrence Berkeley Laboratory and the STAR collaboration, private communication, 2003.

[Zwe64] G. Zweig, CERN preprints Th. 401 and 412, (1964).

Appendix

A.1 Kinematic Variables

Rapidity is related to velocity, as the name implies. It is dimensionless, and describes the rate at which a particle is moving with respect to a reference point on the line of motion. Rapidity is often used as one of the kinetic variables in high-energy collisions. It has the advantage of being additive under Lorentz transformations. Rapidity is defined as [Won94]:

$$y \equiv \frac{1}{2}\ln\left(\frac{E+p_z}{E-p_z}\right) \qquad \{A1\}$$

where:

E is the total energy of the particle and

p_z is the z component of the momentum.

Unlike velocity, rapidity is not a 3 dimensional vector; it s a scalar quantity associated with the *z-axis*. E and p_z can be expressed in terms of rapidity as follows:

$$E^2 = p^2 + E_0^2 = m_t^2 + p_z^2 \qquad \{A2\}$$

where:

$$p^2 = p_x^2 + p_y^2 + p_z^2 \text{ and } m_t^2 = E_0^2 + p_x^2 + p_y^2 \qquad \{A3\}$$

we can see that m_t, the transverse mass, is Lorentz invariant, since p_x and p_y are perpendicular to the beam axis and E_0 is a constant. Finally, from the above relations we are able to express E and p_z in rapidity with the relations:

$$E = m_t \cosh y \text{ and } p_z = m_t \sinh y \qquad \{A4\}$$

We can now re-write {A1} as:

$$y \equiv \frac{1}{2}\ln\left(\frac{1+\beta\cos\theta}{1-\beta\cos\theta}\right) \qquad \{A5\}$$

where:

β is defined as the velocity divided by the speed of light; $\beta = v/c$ and

θ is the particle's angle with respect to the beam axis.

If we take the limit of {A5} as $\beta \to 1$ we can derive a related quantity called the pseudo-rapidity:

$$\eta \equiv -\ln\tan\left(\frac{\theta}{2}\right). \qquad \{A6\}$$

In practice, it is much easier to measure the pseudo-rapidity of a particle since you only need knowledge of the angle of emission, while rapidity requires knowledge of the particle's angle and velocity.

A.2 Glossary of Terms

A

Accelerator

A machine used to accelerate particles to high speeds (and thus high energy compared to their rest mass-energy).

Annihilation

A process in which a particle meets its corresponding antiparticle and both disappear. The energy appears in some other form, perhaps as a different particle and its antiparticle (and their energy), perhaps as many mesons, perhaps as a single neutral boson such as a Z^0 boson. The produced particles may be any combination allowed by conservation of energy and momentum and of all the charge types and other rules.

Anti-matter

Material made from anti-fermions. We define the fermions that are common in our universe as matter and their antiparticles as antimatter. In the particle theory there is no *a priori* distinction between matter and antimatter. The asymmetry of the universe between these two classes of particles is a deep puzzle for which we are not yet completely sure of an explanation.

Anti-particle

For every fermion type there is another fermion type that has exactly the same mass but the opposite value of all other quantum numbers. This is called the antiparticle. For example, the antiparticle of an electron is a particle of positive electric charge called the positron. Bosons also have antiparticles, except for those that have zero value for all charges, for example, a photon or a composite boson made from a quark and its corresponding anti-quark. In this case there is no distinction between the particle and the antiparticle; they are the same object.

Anti-quark

The antiparticle of a quark. An anti-quark is denoted by putting a bar over the corresponding quark ($\bar{d}$, $\bar{u}$, $\bar{s}$, etc.).

B

Beam

The particle stream produced by an accelerator; usually clustered in bunches.

Beam pipe

The particle bunches in the accelerator travel in a vacuum in metal structures called beam pipes. All the air must be removed, or the particles would collide with the air molecules and would lose their energy and direction very quickly.

Boson

A particle that has integer intrinsic angular momentum (spin) measured in units of $\hbar$ (spin = 0, 1, 2,...). All particles are either fermions or bosons. The particles associated with all the fundamental interactions (forces) are bosons. Composite particles with even numbers of fermion constituents (quarks) are also bosons.

C

Calorimeter

A device that can measure the energy deposited in it (originally devices to measure heat energy deposited, using change of temperature; particle physicists use the word for any energy measuring device).

Charge

A quantum number carried by a particle. Determines whether the particle can participate in an interaction process. A particle with electric charge has electrical interactions; one with strong charge has strong interactions, etc.

Collider

An accelerator in which two beams traveling in opposite directions are steered together to provide high-energy collisions between the particles in one beam and those in the other.

Color charge

The quantum number that determines participation in strong interactions, quarks and gluons carry non-zero color charges.

Color neutral

An object with no net color charge. For composites made of color charged particles the rules of neutralization are complex. Three quarks (baryon) or a quark plus an anti-quark (meson) can both form color-neutral combinations.

Confinement

The property of the strong interactions that quarks or gluons are never found separately but only inside color-neutral composite objects.

Conservation

When a quantity (*e.g.*- electric charge, energy or momentum) is conserved, it is the same after a reaction between particles as it was before.

D

Decay

A process in which a particle disappears and in its place two or more different particles appear. The sum of the masses of the produced particles is always less than the mass of the original particle.

Detector

Any device used to sense the passage of a particle. Also a collection of such devices designed so that each serves a particular purpose in allowing physicists to reconstruct collision events.

Down quark

The second flavor of quark (in order of increasing mass), with electric charge -1/3.

E

Electromagnetic Calorimeter

This is a dense and finely instrumented metal structure that measures the position and energy of electrons and photons.

Electromagnetic interaction

The interaction due to electric charge; this includes magnetic effects which have to do with moving electric charges.

Electron

The least massive electrically charged particle, hence absolutely stable. It is the most common lepton, with electric charge -1.

Electroweak interaction

In the Standard Model, electromagnetic and weak interactions are related (unified), physicists use the term electroweak to encompass both of them.

Event

What occurs when two particles collide or a single particle decays. Particle theories predict the probabilities of various possible events occurring when many similar collisions or decays are studied. They cannot predict the outcome for any single event.

F

Fermion

Any particle that has odd-half-integer (1/2, 3/2, ...) intrinsic angular momentum (spin), measured in units of $\hbar$. As a consequence of this peculiar angular momentum, fermions obey a rule called the Pauli Exclusion Principle, which states that no two fermions can exist in the same state at the same place and time. Many of the properties of ordinary matter arise because of this rule. Electrons, protons and neutrons are all fermions, as are all the fundamental matter particles, both quarks and leptons.

Fixed-target experiment

An experiment in which the beam of particles from an accelerator is directed at a stationary (or nearly stationary) target. The target may be a solid, a tank containing liquid or gas, or a gas jet.

Flavor

The name used for the different quark types (*up, down, strange, charm, bottom, top*) and for the different lepton types (*electron, muon, tau*). For each charged lepton flavor there is a corresponding *neutrino* flavor. In other words, flavor is the quantum number that distinguishes the different quark/lepton types. Each flavor of quark and charged lepton has a different mass.

Fundamental interaction

In the Standard Model the fundamental interactions are the strong, electromagnetic, weak and gravitational interactions. There is at least one more fundamental interaction in the theory that is responsible for fundamental particle masses. Five interaction types are all that are needed to explain all observed physical phenomena.

Fundamental particle

A particle with no internal substructure. In the Standard Model the quarks, leptons, photons, gluons, $W^{\pm}$ bosons, and Z^0 bosons are fundamental. All other objects are made from these.

G

Generation

A set of one of each charge type of quark and lepton, grouped by mass. The first generation contains the *up* and *down* quarks, the electron and the electron neutrino.

Gluon

The carrier particle of strong interactions.

H

Hadron

A particle made of strongly-interacting constituents (quarks and/or gluons). These include the mesons and baryons. Such particles participate in residual strong interactions.

Hadronic Calorimeter

This measures the energy and position of strongly interacting particles like pions, kaons, and protons. The Hadronic Calorimeter must be very large and very dense to collect all the energy of particles that interact in it.

Higgs boson

The carrier particle or quantum excitation of the additional force needed to introduce particle masses in the Standard Model. Not yet observed.

Histograms

Histograms are a way of presenting information about the relative frequency of different values of a particular variable. The horizontal axis shows the range of that variable; it is divided into a number of bins -- successive intervals of the value, so a particular observation will fall in one of the bins like letters into a bin in the post office. The vertical axis represents how many times a particular value of the variable has been observed to fall in a particular bin. Cases where the value of the variable is below the low edge of the lowest bin are "underflows", and when the value is higher than the high edge of the highest bin it is an "overflow".

I

Interaction

A process in which a particle decays or it responds to a force due to the presence of another particle (as in a collision). Also used to mean the underlying property of the theory that causes such effects.

J

Jet

Depending on their energy, the quarks and gluons emerging from a collision will materialize into particles (mostly mesons and baryons). At high momentum, these particles will appear in clusters called ``jets," that is, in groups of particles moving in roughly the same direction, centered about the original quark or gluon.

K

Kaon

A meson that is composed of an up quark and a strange quark (for charged kaons $K^+ = u\bar{s}$ and $K^- = \bar{u}s$) or a down quark and a strange quark (for neutral quarks $K^0 = d\bar{s}$ and $\bar{K}^0 = \bar{d}s$).

L

Lepton

A fundamental fermion that does not participate in strong interactions. The electrically-charged leptons are the *electron* (e), the *muon* (μ), the *tau* (τ), and their antiparticles. Electrically-neutral leptons are called *neutrinos* (υ).

LHC

The Large Hadron Collider at the CERN laboratory in Geneva, Switzerland. LHC will collide protons into protons at a center-of-mass energy of about 14 TeV.

Linac

An abbreviation for linear accelerator, that is an accelerator that is has no bends in it. One of the most famous of these is SLAC

M

Mass

see rest mass.

Meson

A hadron made from an even number of quark constituents. The basic structure of most mesons is one quark and one antiquark.

Muon

The second flavor of charged lepton (in order of increasing mass), with electric charge -1.

N

Neutral

Having a net charge equal to zero. Unless specified otherwise, it usually refers to electric charge.

Neutrino

A lepton with no electric charge. Neutrinos participate only in weak and gravitational interactions and therefore are very difficult to detect. There are three known types of neutrino all of which are very light.

Neutron

A baryon with electric charge zero; it is a fermion with a basic structure of two *down* quarks and one *up* quark (held together by gluons). The neutral component of an atomic nucleus is made from neutrons. Different isotopes of the same element are distinguished by having different numbers of neutrons in their nucleus.

Nucleon

A proton or a neutron; that is, one of the particles that makes up a nucleus.

Nucleus

A collection of neutrons and protons that forms the core of an atom.

O

P

Particle

A subatomic object with a definite mass and charge.

Parton

An elementary particle, such as quarks and gluons, that make up hadrons.

Photon

The carrier particle of electromagnetic interactions.

Pion

The least massive type of meson, pions can have electric charges ± 1 or 0.

Plasma

A gas of charged particles.

Positron

The antiparticle of the electron.

Proton

The most common hadron, a baryon with electric charge (+1) equal and opposite to that of the electron (-1). Protons have a basic structure of two *up* quarks and one *down* quark (bound together by gluons). The nucleus of a hydrogen atom is a proton. A nucleus with electric charge Z contains Z protons; therefore the number of protons is what distinguishes the different chemical elements.

Q

Quantum

The smallest discrete amount of any quantity.

Quantum mechanics

The laws of physics that apply on very small scales. The essential feature is that energy, momentum, and angular momentum as well as charges come in discrete amounts called *quanta*.

Quark

A fundamental fermion that has strong interactions. Quarks have electric charge of either 2/3 (*up, charm, top*) or -1/3 (*down, strange, bottom*) in units where the proton charge is 1.

R

Rest mass

The rest mass (m) of a particle is the mass defined by the energy of the isolated (free) particle at rest, divided by c^2. When particle physicists use the word ``mass," they always mean the ``rest mass" (m) of the object in question. The total energy of a free particle is given by $E = \sqrt{p^2c^2 + m^2c^4}$ where p is the momentum of the particle. Note that for p=0 this simplifies to Einstein's famous $E = mc^2$.

S

SLAC

The Stanford Linear Accelerator Center in Stanford, California.

Spin

Intrinsic angular momentum of a particle, given in units of $\hbar$, the quantum unit of angular momentum, where $\hbar = h/2\pi$.

Standard Model

Physicists' name for the theory of fundamental particles and their interactions. It has been widely tested and is generally accepted as correct by particle physicists.

Strange quark

The third flavor of quark (in order of increasing mass), with electric charge -1/3.

Strong interaction

The interaction responsible for binding quarks, anti-quarks, and gluons to make hadrons. Residual strong interactions provide the nuclear binding force.

Subatomic particle

Any particle that is small compared to the size of the atom.

Synchrotron

A type of circular accelerator in which the particles travel in synchronized bunches at fixed radius.

T

Track

The record of the path of a particle traversing a detector.

Tracking

The reconstruction of a ``track'' left in a detector by the passage of a particle through the detector.

U

Up quark:

The least massive flavor of quark, with electric charge 2/3.

V

Vertex detector

A detector placed very close to the collision point in a colliding beam experiment so that tracks coming from the decay of a short-lived particle produced in the collision can be accurately reconstructed and seen to emerge from a `vertex' point that is different from the collision point.

W

$W^{\pm}$ boson

A carrier particle of the weak interactions. It is involved in all electric-charge-changing weak processes.

Weak interaction

The interaction responsible for all processes in which flavor changes, hence for the instability of heavy quarks and leptons, and particles that contain them. Weak interactions that do not change flavor (or charge) have also been observed.

X

Y

Z

Z^0 boson

A carrier particle of weak interactions. It is involved in all weak processes that do not change flavor.

A.3 Acronyms

AGS Alternating Gradient Synchrotron. High energy accelerator built in the late 1950's. Now serves part-time as an accelerator-injector for RHIC.

CTB Central Trigger Barrel. Scintillation detector located outside the TPC, used for fast event triggering; see section 3.2.2.

DAQ Data Acquisition System. System that collects data from the STAR detectors and sends it to the HPSS; see section 4.

EMC Electromagnetic Calorimeter. Designed to measure direct photons, jets, and high p_t particle spectra.

FTPC Forward Time Projection Chamber. Designed to extend the coverage of STAR into the very forward region; see section 3.2.2.

HEP High Energy Physics

HPSS High Performance Storage System. Collection of hardware designed for high-speed high-storage capacity; see section 4.

MWPC Multi-Wire Proportional Chamber. Readout system employed by the TPC.

P10 TPC gas mixture of 90% Argon + 10% Methane; see section 5.2.1.

QCD Quantum Chromodynamics. A theory of matter, based on the assumption that quarks are distinguished by differences in color and are held together by gluons.

QGP Quark-Gluon Plasma. A predicted phase of matter consisting of "free" quarks and gluons. May have existed a few milliseconds after the Big Bang, and possibly in the center of neutron stars.

RHIC Relativistic Heavy Ion Collider. Collider located at Brookhaven National Laboratory on Long Island, NY; see section 3.1.

STAR Solenoidal Tracker at RHIC. A collection of detectors located at RHIC; see section 3.2.

SVT Silicon Vertex Tracker. High resolution detector located very near the beamline at z=0; see section 3.2.2.

TPC Time Projection Chamber. The primary tracking detector in STAR. It is a ionization drift detector 4.2 m long and 4 m outer radius; see section 3.2.1.

ZDC Zero Degree Calorimeter. RHIC common trigger detector, located ~±18 m downstream from z=0; see section 3.2.2.

A.4 STAR Collaboration Author List

J. Adams,[3] C. Adler,[12] M.M. Aggarwal,[25] Z. Ahammed,[38] J. Amonett,[17] B.D. Anderson,[17] M. Anderson,[5] D. Arkhipkin,[11] G.S. Averichev,[10] S.K. Badyal,[16] J. Balewski,[13] O. Barannikova,[28 , 10] L.S. Barnby,[17] J. Baudot,[15] S. Bekele,[24] V.V. Belaga,[10] R. Bellwied,[41] J. Berger,[12] B.I. Bezverkhny,[43] S. Bhardwaj,[29] P. Bhaskar,[38] A.K. Bhati,[25] H. Bichsel,[40] A. Billmeier,[41] L.C. Bland,[2] C.O. Blyth,[3] B.E. Bonner,[30] M. Botje,[23] A. Boucham,[34] A. Brandin,[21] A. Bravar,[2] R.V. Cadman,[1] X.Z. Cai,[33] H. Caines,[43] M. Calderón de la Barca Sánchez,[2] J. Carroll,[18] J. Castillo,[18] M. Castro,[41] D. Cebra,[5] P. Chaloupka,[9] S. Chattopadhyay,[38] H.F. Chen,[32] Y. Chen,[6S] .P. Chernenko,[10] M. Cherney,[8] A. Chikanian,[43] B. Choi,[36] W. Christie,[2] J.P. Coffin,[15] T.M. Cormier,[41] J.G. Cramer,[40] H.J. Crawford,[4] D. Das,[38] S. Das,[38] A.A. Derevschikov,[27] L. Didenko,[2] T. Dietel,[12] X. Dong,[32 , 18] J.E. Draper,[5] F. Du,[43] A.K. Dubey,[14] V.B. Dunin,[10] J.C. Dunlop,[2] M.R. Dutta Majumdar,[38] V. Eckardt,[19] L.G. E_mov,[10] V. Emelianov,[21] J. Engelage,[4] G. Eppley,[30] B. Erazmus,[34] M. Estienne,[34] P. Fachini,[2] V. Faine,[2] J. Faivre,[15] R. Fatemi,[13] K. Filimonov,[18] P. Filip,[9] E. Finch,[43] Y. Fisyak,[2] D. Flierl,[12] K.J. Foley,[2] J. Fu,[42] C.A. Gagliardi,[35] M.S. Ganti,[38] T.D. Gutierrez,[5] N. Gagunashvili,[10] J. Gans,[43] L. Gaudichet,[34] M. Germain,[15] F. Geurts,[30] V. Ghazikhanian,[6] P. Ghosh,[38] J.E. Gonzalez,[6] O. Grachov,[41] V. Grigoriev,[21] S. Gronstal,[8] D. Grosnick,[37] M. Guedon,[15] S.M. Guertin,[6] A. Gupta,[16] E. Gushin,[21] T.J. Hallman,[2] D. Hardtke,[18] J.W. Harris,[43] M. Heinz,[43] T.W. Henry,[35] S. Heppelmann,[26] T. Herston,[28] B. Hippolyte,[43] A. Hirsch,[28] E. Hjort,[18] G.W. Ho_mann,[36] M. Horsley,[43] H.Z. Huang,[6] S.L. Huang,[32] T.J. Humanic,[24] G. Igo,[6] A. Ishihara,[36] P. Jacobs,[18] W.W. Jacobs,[13] M. Janik,[39] I. Johnson,[18] P.G. Jones,[3] E.G. Judd,[4] S. Kabana,[43] M. Kaneta,[18] M. Kaplan,[7] D. Keane,[17] J. Kiryluk,[6] A. Kisiel,[39] J. Klay,[18] S.R. Klein,[18] A. Klyachko,[13] D.D. Koetke,[37] T. Kollegger,[12] A.S. Konstantinov,[27] M. Kopytine,[17] L. Kotchenda,[21] A.D. Kovalenko,[10] M. Kramer,[22] P. Kravtsov,[21] K. Krueger,[1] C. Kuhn,[15] A.I. Kulikov,[10] A. Kumar,[25] G.J. Kunde,[43] C.L. Kunz,[7] R.Kh. Kutuev,[11] A.A. Kuznetsov,[10] M.A.C. Lamont,[3] J.M. Landgraf,[2] S. Lange,[12] C.P. Lansdell,[36] B. Lasiuk,[43] F. Laue,[2] J. Lauret,[2] A. Lebedev,[2] R. Lednický,[10] V.M. Leontiev,[27] M.J. LeVine,[2] C. Li,[32] Q. Li,[41] S.J. Lindenbaum,[22] M.A. Lisa,[24] F. Liu,[42] L. Liu,[42] Z. Liu,[42] Q.J. Liu,[40] T. Ljubicic,[2] W.J. Llope,[30] H. Long,[6] R.S. Longacre,[2] M. Lopez-Noriega,[24] W.A. Love,[2] T. Ludlam,[2] D. Lynn,[2] J. Ma,[6] Y.G. Ma,[33] D. Magestro,[24] S. Mahajan,[16] L.K. Mangotra,[16] D.P. Mahapatra,[14] R. Majka,[43] R. Manweiler,[37] S. Margetis,[17] C. Markert,[43] L. Martin,[34] J. Marx,[18] H.S. Matis,[18] Yu.A. Matulenko,[27] T.S. McShane,[8] F. Meissner,[18] Yu. Melnick,[27] A. Meschanin,[27] M. Messer,[2] M.L. Miller,[43] Z. Milosevich,[7] N.G. Minaev,[27] C. Mironov,[17] D.Mishra,[14] J. Mitchell,[30] B. Mohanty,[38] L. Molnar,[28] C.F. Moore,[36] M.J. Mora-Corral,[19] V. Morozov,[18] M.M. deMoura,[41] M.G. Munhoz,[31] B.K. Nandi,[38] S.K. Nayak,[16] T.K. Nayak,[38] J.M. Nelson,[3] P. Nevski,[2] V.A. Nikitin,[11] L.V. Nogach,[27] B. Norman,[17] S.B. Nurushev,[27] G. Odyniec,[18] A. Ogawa,[2] V. Okorokov,[21] M. Oldenburg,[18] D. Olson,[18] G. Paic,[24] S.U. Pandey,[41] S.K. Pal,[38] Y. Panebratsev,[10] S.Y. Panitkin,[2] A.I. Pavlinov,[41] T. Pawlak,[39] V. Perevoztchikov,[2] W. Peryt,[39] V.A. Petrov,[11] S.C. Phatak,[14] R. Picha,[5] M. Planinic,[44] J. Pluta,[39] N. Porile,[28] J. Porter,[2] A.M. Poskanzer,[18] M. Potekhin,[2] E. Potrebenikova,[10] B.V.K.S. Potukuchi,[16] D. Prindle,[40] C. Pruneau,[41] J. Putschke,[19] G. Rai,[18] G. Rakness,[13] R. Raniwala,[29] S. Raniwala,[29] O. Ravel,[34] R.L. Ray,[36] S.V. Razin,[10,13] D. Reichhold,[28] J.G. Reid,[40] G. Renault,[34] F. Retiere,[18] A. Ridiger,[21] H.G. Ritter,[18] J.B. Roberts,[30] O.V. Rogachevski,[10] J.L. Romero,[5] A. Rose,[41] C. Roy,[34] L.J. Ruan,[32,2] R. Sahoo,[14] I. Sakrejda,[18] S. Salur,[43] J. Sandweiss,[43] I. Savin,[11] J. Schambach,[36] R.P. Scharenberg,[28] N. Schmitz,[19] L.S. Schroeder,[18] K. Schweda,[18] J. Seger,[8] D. Seliverstov,[21] P. Seyboth,[19] E. Shahaliev,[10] M. Shao,[32] M. Sharma,[25] K.E. Shestermanov,[27] S.S. Shimanskii,[10] R.N. Singaraju,[38] F. Simon,[19] G. Skoro,[10] N. Smirnov,[43] R. Snellings,[23] G. Sood,[25] P. Sorensen,[6] J. Sowinski,[13] H.M. Spinka,[1] B. Srivastava,[28] S. Stanislaus,[37] R. Stock,[12] A. Stolpovsky,[41] M. Strikhanov,[21] B. Stringfellow,[28] C. Struck,[12] A.A.P. Suaide,[41] E. Sugarbaker,[24] C. Suire,[2] M. Šumbera,[9] B. Surrow,[2] T.J.M. Symons,[18] A. Szanto de Toledo,[31] P. Szarwas,[39] A. Tai,[6] J. Takahashi,[31] A.H. Tang,[2,23] D. Thein,[6] J.H. Thomas,[18] V. Tikhomirov,[21] M. Tokarev,[10] M.B. Tonjes,[20] T.A. Trainor,[40] S. Trentalange,[6] R.E. Tribble,[35] M.D. Trivedi,[38] V. Tro_mov,[21] O. Tsai,[6] T. Ullrich,[2] D.G. Underwood,[1] G. Van Buren,[2] A.M. VanderMolen,[20] A.N. Vasiliev,[27] M. Vasiliev,[35] S.E. Vigdor,[13] Y.P. Viyogi,[38] S.A. Voloshin,[41] W. Waggoner,[8] F. Wang,[28] G. Wang,[17] X.L. Wang,[32] Z.M. Wang,[32] H. Ward,[36] J.W. Watson,[17] R. Wells,[24] G.D. Westfall,[20] C. Whitten Jr.,[6] H. Wieman,[18] R. Willson,[24] S.W. Wissink,[13] R. Witt,[43] J. Wood,[6] J. Wu,[32] N. Xu,[18] Z. Xu,[2] Z.Z. Xu,[32] A.E. Yakutin,[27] E. Yamamoto,[18] J. Yang,[6] P. Yepes,[30] V.I. Yurevich,[10] Y.V. Zanevski,[10] I. Zborovský,[9] H. Zhang,[43,2] H.Y. Zhang,[17] W.M. Zhang,[17] Z.P. Zhang,[32] P.A. Żołnierczuk,[13] R. Zoulkarneev,[11] J. Zoulkarneeva,[11] and A.N. Zubarev[102]

(STAR Collaboration)*,

[1]Argonne National Laboratory, Argonne, Illinois 60439

[2]Brookhaven National Laboratory, Upton, New York 11973
[3]University of Birmingham, Birmingham, United Kingdom
[4]University of California, Berkeley, California 94720
[5]University of California, Davis, California 95616
[6]University of California, Los Angeles, California 90095
[7]Carnegie Mellon University, Pittsburgh, Pennsylvania 15213
[8]Creighton University, Omaha, Nebraska 68178
[9]Nuclear Physics Institute AS CR, Řež/Prague, Czech Republic
[10]Laboratory for High Energy (JINR), Dubna, Russia
[11]Particle Physics Laboratory (JINR), Dubna, Russia
[12]University of Frankfurt, Frankfurt, Germany
[13]Indiana University, Bloomington, Indiana 47408
[14]Insitute of Physics, Bhubaneswar 751005, India
[15]Institut de Recherches Subatomiques, Strasbourg, France
[16]University of Jammu, Jammu 180001, India
[17]Kent State University, Kent, Ohio [44242]
[18]Lawrence Berkeley National Laboratory, Berkeley, California 94720
[19]Max-Planck-Institut f. ur Physik, Munich, Germany
[20]Michigan State University, East Lansing, Michigan 48824
[21]Moscow Engineering Physics Institute, Moscow Russia
[22]City College of New York, New York City, New York 10031
[23]NIKHEF, Amsterdam, The Netherlands
[24]Ohio State University, Columbus, Ohio 43210
[25]Panjab University, Chandigarh 160014, India
[26]Pennsylvania State University, University Park, Pennsylvania 16802
[27]Institute of High Energy Physics, Protvino, Russia
[28]Purdue University, West Lafayette, Indiana 47907
[29]University of Rajasthan, Jaipur 302004, India
[30]Rice University, Houston, Texas 77251
[31]Universidade de Sao Paulo, Sao Paulo, Brazil
[32]University of Science & Technology of China, Anhui 230027, China
[33]Shanghai Institute of Nuclear Research, Shanghai 201800, P.R. China
[34]SUBATECH, Nantes, France
[35]Texas A&M, College Station, Texas 77843
[36]University of Texas, Austin, Texas 78712
[37]Valparaiso University, Valparaiso, Indiana 46383
[38]Variable Energy Cyclotron Centre, Kolkata 700064, India
[39]Warsaw University of Technology, Warsaw, Poland
[40]University of Washington, Seattle, Washington 98195
[41]Wayne State University, Detroit, Michigan 48201
[42]Institute of Particle Physics, CCNU (HZNU), Wuhan, 430079 China
[43]Yale University, New Haven, Connecticut 06520
[44]University of Zagreb, Zagreb, HR-10002, Croatia

----

*URL: www.star.bnl.gov